Gonzalez-Blanco, L. & Romero, E. *Géotechnique* [https://doi.org/10.1680/jgeot.21.00208]

A multi-scale insight into gas transport in a deep Cenozoic clay

LAURA GONZALEZ-BLANCO*† and ENRIQUE ROMERO*‡

The migration of gases is crucial to ensure the long-term feasibility of argillaceous formations for the deep disposal of radioactive waste. This paper presents an experimental investigation with a multi-scale perspective on the response to gas transport of initially saturated Boom Clay (Belgium). Gas injection tests have been performed under oedometer conditions at different controlled-volume rates, constant total vertical stress and different sample orientations (flow orthogonal or parallel to bedding planes). The results confirm soil expansion and consequent degradation during injection that has a significant impact on the aperture of localised gas pathways (fissures) and increases intrinsic permeability during the gas pressure dissipation stage. The analyses with complementary techniques (mercury intrusion porosimetry, field-emission scanning electron microscopy and X-ray micro-tomography) confirm the opening of fissures with different apertures and separations at the microstructural scale. Large-aperture fissures develop along the weaker bedding planes. These techniques allow the volume of fissures to be quantified, which does not significantly depend on gas flow direction, as also measured in the isotropic response of the gas effective permeability. A scalar damage variable derived from the fissured fraction has been used to assess the gas-entry pressure reduction and the intrinsic permeability increase after the gas tests in both directions.

KEYWORDS: fabric/structure of soils; laboratory tests; permeability; radioactive waste disposal; soft rocks

INTRODUCTION AND BACKGROUND

Gas transport issues are increasingly gaining importance in energy-related geotechnics, such as carbon capture and storage, the production of shale gas, and deep geological disposal of radioactive waste (e.g. Cevatoglu *et al*., 2015). With regard to the latter, underground repositories remain the preferred option for managing long-living and heat-emitting radioactive wastes, confining the wastes in a deep argillaceous geological formation for very long periods (e.g. Bernier *et al*., 2007; Giger *et al*., 2015). Therefore, assessing the long-term phenomena and understanding the long-term behaviour of rocks are essential issues to ensure the feasibility of geological disposal facilities. One of these long-term phenomena is the generation of gases that may impair the geological formation due to several processes, including the anaerobic corrosion of the metallic parts in the disposal (Volckaert *et al*., 1998). A recent European joint programme has been launched to improve the understanding and predictability of gas transport in different argillaceous host rocks (EURAD, 2019). A crucial aspect is the coupling with the mechanical behaviour and the impact on the host rock properties associated with the creation of gas pathways (Delahaye & Alonso, 2002; Jockwer & Wieczorek, 2008; Olivella & Alonso, 2008; Gerard *et al*., 2014; Wiseall *et al*., 2015; Gonzalez-Blanco *et al*., 2016, 2022; Harrington *et al*., 2019). These gas pathways may develop through interfaces between the engineered and natural components, or taking advantage of the weakest zones, whether inherent to the rock (bedding planes, low-density zones, or rock discontinuities) or caused by previously damaged zones with increased permeability around excavations.

Laboratory campaigns have been traditionally focused on determining the gas breakthrough pressure (e.g. Harrington & Horseman, 1999; Hildenbrand *et al*., 2004; Gutiérrez-Rodrigo *et al*., 2015; Wiseall *et al*., 2015; Villar *et al*., 2019; Cui *et al*., 2020). Only recently have authors recognised the importance of coupling the deformational response and the gas pressure (Romero *et al*., 2012; Cuss *et al*., 2014; Senger *et al*., 2014; Romero & Gonzalez-Blanco, 2015; Liu *et al*., 2016b; Harrington *et al*., 2017; Senger *et al*., 2018; Gonzalez-Blanco *et al*., 2022). Gas injection experiments at constant total stress systematically display expansion deformations that induce damage to the rock and the opening of preferential gas pathways (Gonzalez-Blanco *et al*., 2016, 2022). Notwithstanding all these efforts, there are still many experimental aspects to be addressed. To cite some of them: the tracking of the gas pathways, particularly when connecting between bedding planes orthogonal to flow; the determination of the displaced water on gas injection; and the changes in intrinsic permeability and gas entry pressure that depend on the mechanical degradation of the argillaceous rock. Specifically, the aim of this paper is to study this last topic, in which microstructural information is essential to provide evidence on the opening and volume of these gas pathways. The dependence of the effective gas permeability (ability to flow when water is present), which is independent of fluid properties, on the initial fabric of compacted clays has been recently described by Nguyen *et al*. (2021), and the potential pore space relevant to gas permeability has been addressed by Keller *et al*. (2013). Nevertheless, to the authors' best knowledge, there are limited data in the literature on the geometry of these gas pathways (aperture and separation of pathways) and their volume in argillaceous rocks after a gas

Manuscript received 30 July 2021; revised manuscript accepted 12 May 2022.
Discussion on this paper is welcomed by the editor.

* Geomechanics Group, International Centre for Numerical Methods in Engineering (CIMNE), Barcelona, Spain.
† Division of Geotechnical Engineering and Geosciences, Department of Civil and Environmental Engineering, Universitat Politècnica de Catalunya, Barcelona, Spain (Orcid:0000-0003-3800-3007).
‡ Division of Geotechnical Engineering and Geosciences, Department of Civil and Environmental Engineering, Universitat Politècnica de Catalunya, Barcelona, Spain (Orcid:0000-0002-4105-8941).

injection test, except for the results presented by Harrington *et al.* (2012). They detected minimum apertures ranging between 0·5 and 10 μm using nanoparticle injection. These gas pathways generated by rock degradation are different to the connected pore network of the intrinsic permeability to water.

The microstructural information before and after gas injection is also helpful for using advanced numerical models that allow coupling the gas transport properties to the mechanical response of the degraded material. For example, some numerical approaches have considered an embedded fracture model with pressure-dependent pathways (Olivella & Alonso, 2008; Arnedo *et al.*, 2013; Gerard *et al.*, 2014; Gonzalez-Blanco *et al.*, 2016; Damians *et al.*, 2019). Other authors have used a Klinkenberg-type equation for implementing gas-pressure-dependent permeability associated with pathway dilation and micro-fracturing in argillaceous materials (Senger *et al.*, 2008, 2018). In contrast, other authors (Pereira & Arson, 2013; Fall *et al.*, 2014; Yang & Fall, 2021) define a damage variable accounting for the microscopic degradation of a representative elementary volume (REV) that affects the intrinsic permeability to gas. There is, therefore, a need to generate a good quality database on the microstructural changes induced by gas injection to allow further development and validation of these models.

This paper presents an innovative multi-scale experimental programme to capture the opening of preferential pathways and assess the volume of fissures after gas injection tests in Boom Clay (BC), a Cenozoic plastic argillaceous rock candidate to host the radioactive wastes in Belgium (Bernier *et al.*, 2007). Gas injection and dissipation tests under oedometer conditions on fully saturated samples at different orientations of bedding planes and constant total vertical stress were performed. In addition, the geometric properties of the gas pathways (aperture, separation and volume of fissures) were studied using different microstructural techniques to cover a wide range of pore/fissure sizes (mercury intrusion porosimetry (MIP), field-emission scanning electron microscopy (FESEM) and micro-focus X-ray computed tomography (μCT)). An effort will be made at the end of the paper to combine the gas injection/dissipation data and the microstructural information to analyse the effects on the gas transport properties (intrinsic permeability and gas entry value), as well as to determine the potential desaturation of the material after gas passage.

MATERIAL AND OEDOMETER CELL

The BC is a marine plastic clay formation of the Rupelian age (34 to 28 Ma) located between 190 and 290 m depth at the Mol-Dessel site (Belgium). The mineralogical composition is 20–30% kaolinite, 20–30% illite, 10–20% smectite and 25% quartz and feldspar. Further details can be found in Bernier *et al.* (2007), Delage *et al.* (2007) and Sultan *et al.* (2010). This sedimentary clay presents bedding planes in the horizontal direction, which leads to anisotropic features (Lima, 2011; Salehnia *et al.*, 2015; Gonzalez-Blanco *et al.*, 2017). This markedly anisotropic behaviour associated with the depositional and bedding features has also been reported by Brosse *et al.* (2017) on equivalent plastic clays, which share broadly similar marine conditions and depositional age.

The BC samples were retrieved from the Hades URL Underground Research Laboratory (Mol, Belgium) at 223 m. The total vertical stress and water pressure at the sampling depth are around $\sigma_v = 4{\cdot}6$ MPa and $u_w = 2{\cdot}2$ MPa, respectively. Table 1 summarises the main properties and the initial test conditions (equivalent to in situ conditions).

The drying branch of the water retention curve was obtained using a chilled mirror dew point psychrometer (WP4 Decagon Devices, Inc.) by stepwise drying starting from the initial total suction and void ratio, $e = 0{\cdot}61$. Shrinkage of the sample was considered by using data reported in Lima (2011), who performed drying tests under isotropic stress conditions using axis translation and the vapour equilibrium technique. Fig. 1 presents the water retention results fitted to van Genuchten's expression (van Genuchten, 1980). The total suction results allowed estimation of an air-entry value of around 4·6 MPa at a degree of saturation $S_r = 0{\cdot}95$. The initial total suction was 2·45 MPa, despite being saturated. BC at the Hades URL presents an overconsolidation ratio (OCR) between 2·1 and 2·3 (Bernier *et al.*, 2007; Delage *et al.*, 2007; Lima, 2011; Dao, 2015; Gonzalez-Blanco *et al.*, 2016), associated with a lateral pressure coefficient at rest K_0 close to 0·9 (Bernier *et al.*, 2007; Dao, 2015; Gonzalez-Blanco *et al.*, 2016). The initial total suction measured is a consequence of the undrained unloading upon sampling, in which matric suction increased, assuming null effective stress change during the process (Delage *et al.*, 2007; Lima, 2011; Gonzalez-Blanco, 2017). This initial suction should be considered to define the stress paths since samples can undergo expansion and possible degradation on contact with water at low stresses (Sultan *et al.*, 2010; Lima, 2011; Bésuelle *et al.*, 2014). For this reason, samples were initially loaded to total vertical stress slightly higher than the in situ effective vertical stress and then placed in contact with synthetically prepared BC water at atmospheric pressure and equivalent osmotic suction (the osmotic

Table 1. Main geotechnical properties and initial state of BC samples

Main properties/initial state	Present study	Lima (2011)
Density of solids, ρ_s: Mg/m^3	2·67	2·67
Liquid limit, w_L: %	67	56
Plastic limit, w_P: %	29	29
Dominant pore size from MIP: nm	70	70–90
Air-entry value (matric suction) from water retention curve: MPa	4·1	—
Bulk density, ρ: Mg/m^3	2·02–2·06	1·99–2·05
Dry density, ρ_d: Mg/m^3	1·63–1·69	1·65–1·71
Water content, w: %	22·6–24·0	21–25
Void ratio, e	0·58–0·63	0·56–0·62
Porosity, n	0·37–0·39	0·36–0·38
Degree of saturation, S_r	Close to 1	0·91–1
Total suction, s: MPa	2·45	2·5–4·0
Osmotic suction, π: MPa	0·5	–

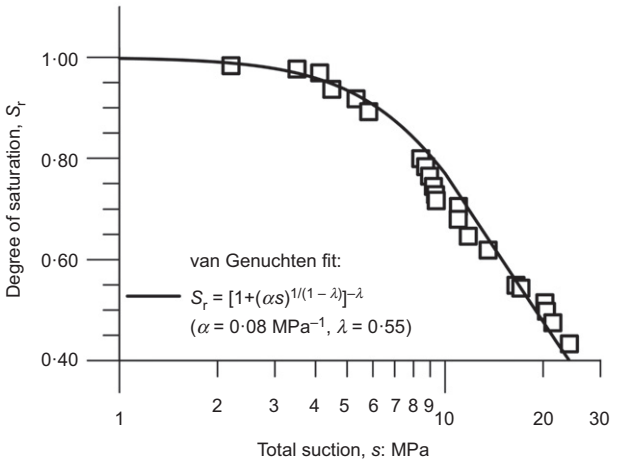

Fig. 1. Drying branch of the water retention curve and fitting with van Genuchten's equation presented in figure

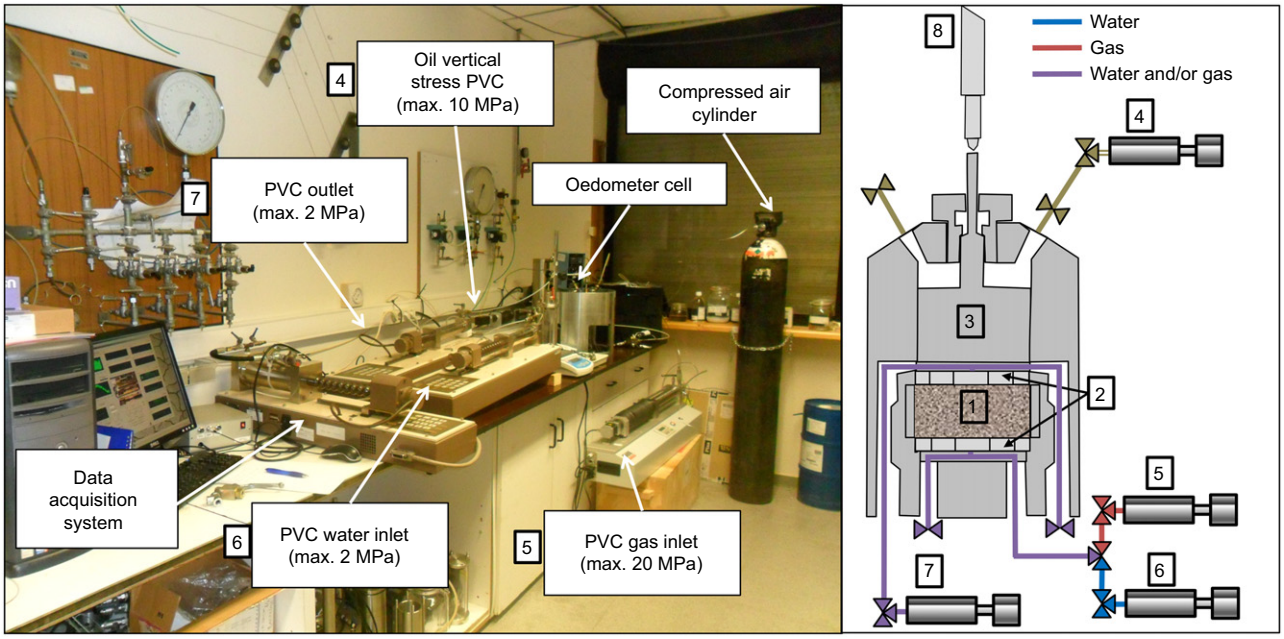

Fig. 2. Photograph and schematic representation of the oedometer set-up: 1, sample; 2, concentric stainless steel rings; 3, vertical hydraulic piston; 4, pressure/volume controller (PVC) for applying vertical stress; 5, inlet PVC for gas; 6, inlet PVC for water; 7, outlet PVC for water and gas recovery; 8, displacement transducer

suction $\pi = 0{\cdot}5$ MPa of this synthetic water was measured with the same psychrometer).

A high-pressure and high-stiffness oedometer cell was used to perform the water permeability and gas injection/dissipation tests. A schematic representation of the cell and a photograph of the set-up are shown in Fig. 2. The sample (20 mm high and 50 mm dia., '1' in the diagram on the right) was placed inside a very stiff oedometer ring and between the bottom and top caps made of concentric stainless steel rings with gaps for the inlet and outlet of water and gas ('2' in the same figure). Vertical total stress was hydraulically applied by a pressure/volume controller (PVC) ('4'), and vertical displacements of the top vertical piston ('3') were measured with an external displacement transducer ('8'). The injection system consisted of two PVCs (upstream boundary at the bottom of the sample), one for gas and another for water ('5' and '6', respectively) using the same drainage cap. In contrast, for the recovery system (top downstream boundary), a unique PVC ('7') was installed to supply the water pressure and collect water and gas during the injection/dissipation stages at constant outflow pressure.

EXPERIMENTAL WORK

Hydro-mechanical paths and microstructural studies

Three introductory hydro-mechanical (HM) paths with three different unloading rates were performed on samples with bedding planes orthogonal to the axis of revolution and three objectives. The first was to study the compressibility on loading of the material – with a degree of saturation close to one – to the maximum total vertical stress $\sigma_v = 6{\cdot}0$ MPa used in the gas tests; the second was to analyse the possible swelling on liquid contact at $\sigma_v = 3{\cdot}0$ MPa; and the finally objective was to check the volume changes at different unloading rates from $\sigma_v = 6{\cdot}0$ MPa to 1·0 MPa. This last objective is relevant because the microstructural tests will be performed on unloaded samples after the gas tests. Therefore, these preliminary HM tests at three different unloading rates were completed with MIP tests (Delage *et al.*, 1996; Romero & Simms, 2008; Matthews *et al.*, 2018) to understand how the pore size density functions (PSDs) were affected. The tests were carried out in an auxiliary oedometer cell with lateral stress measurement (semi-rigid system with oedometer ring keeping radial deformation at a low level $<1 \times 10^{-2}\%$ MPa^{-1}).

A first loading stage to $\sigma_v = 3{\cdot}0$ MPa was carried out at a relatively fast rate of 15 kPa/min and constant water content (paths 'AB' in Fig. 3(a)). The initial matric suction decreased during this fast-loading path due to the total stress change (maximum total horizontal stress was 2·9 MPa). The isotropic pore pressure parameter for an incompressible solid was estimated in $B = 0{\cdot}93$, which is consistent with Giraud & Rousset (1996) and based on the average bulk compressibility of the soil skeleton $2{\cdot}9 \times 10^{-6}$ m^2/kN along the path 'AB'. At $\sigma_v = 3{\cdot}0$ MPa, samples were placed in contact with water at atmospheric pressure at both top and bottom boundaries. Some swelling was recorded during water contact (path 'BC' in Fig. 3(a)), which indicated that small matric suction remained after the water undrained loading (around 0·1 MPa measured on an additional test). The synthetically prepared water displayed the same composition and osmotic suction as the interstitial water (Table 1), and no osmotic effects were expected. After equalisation, water pressure at both boundaries was increased to 0·5 MPa to reach an effective vertical stress approximately equivalent to in situ conditions.

Afterwards, the samples were loaded to $\sigma_v = 6{\cdot}0$ MPa under drained conditions (0·5 kPa/min) while keeping a back-pressure of 0·5 MPa (path 'CD' in Fig. 3(a) with maximum total horizontal stress of 5·2 MPa), and later unloaded to $\sigma_v = 1{\cdot}0$ MPa at different stress rates and constant water pressure of 0·5 MPa at the boundaries (path 'DE' in the figure). The maximum effective vertical stress was close to the yield stress of 5·2 MPa reported by Lima (2011) and Gonzalez-Blanco *et al.* (2016). As observed in Fig. 3(a), despite starting at slightly different initial void ratios (natural variability in Table 1), the compressibility curves to point 'D' displayed the same slopes and change in void ratio. However, the differences in unloading at different stress rates and slightly different void ratios were remarkable. In test HM-1, unloading was carried out at a rate of 0·9 kPa/min, and the sample displayed significant swelling, resulting in a final void

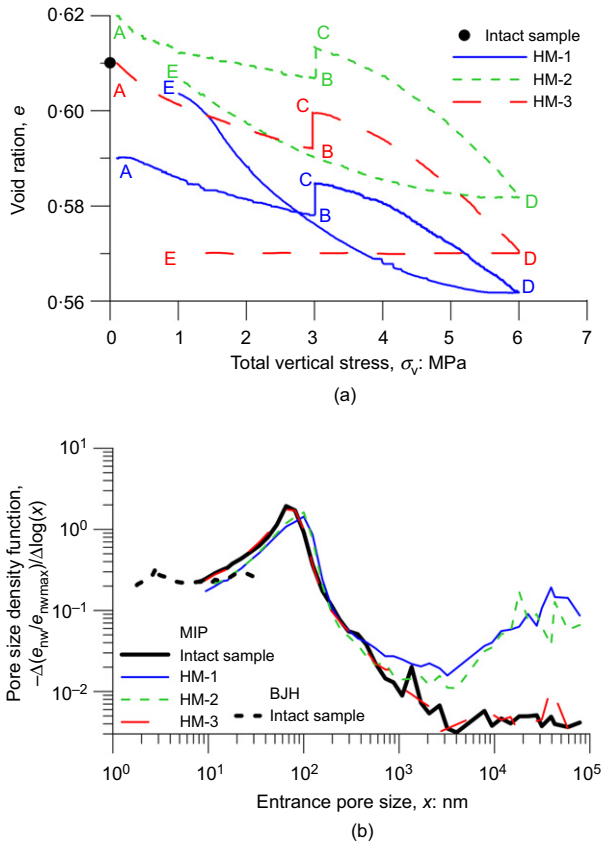

Fig. 3. (a) Deformation response of samples with bedding planes orthogonal to the axis of revolution on loading at constant water content 'AB', on soaking at constant total vertical stress 'BC', on drained loading 'CD', and on unloading at different stress rates 'DE'. (b) Pore size density functions from MIP on the intact sample (complemented with nitrogen (N_2) adsorption using the Barrett, Joyner and Halenda (BJH) method) and after the hydro-mechanical (HM) paths

ratio higher than the initial one ($e_0 = 0{\cdot}59$). In test HM-2 starting at $e_0 = 0{\cdot}62$, unloading was carried out at a faster rate of 30 kPa/min, during which the sample was also able to undergo expansion, reaching approximately the same final void ratio as HM-1. The test HM-3 at $e_0 = 0{\cdot}61$ followed undrained unloading with null expansion since the total vertical stress reduced instantaneously while matric suction increased under constant effective stress. At the end of this test, the matric suction was 4·0 MPa and slightly below the air-entry value (Table 1). This matric suction was determined using the total suction measured with the psychrometer and the osmotic suction of the synthetically prepared BC water. The isotropic pore pressure parameter on unloading was $B = 0{\cdot}83$.

The MIP tests were carried out on freeze-dried samples (intact sample and samples after the unloading paths) to analyse the PSD changes in terms of the intruded volume of mercury referred to the volume of solids (non-wetting void ratio e_{nw}) for different entrance pore sizes x within 7 nm and 400 μm (Romero & Simms, 2008). The PSD of the intact material was completed in the low pore size domain by nitrogen (N_2) adsorption (Barrett, Joyner and Halenda (BJH) method (Webb & Orr, 1997)). The connected void ratio detected by MIP was around 0·50 and increased to $e_{nw\,max} = 0{\cdot}58$ when adding the void ratio identified by nitrogen adsorption (close to the void ratio reported in Table 1). The maximum intruded pore volume $e_{nw\,max}$ has been used in Fig. 3(b) to normalise the original PSD data and better compare the results with slightly different void ratios. In addition, PSDs were plotted in a log–log graph to emphasise the differences at $x > 2$ μm.

As observed in Fig. 3(b), the intact BC presented a mono-modal PSD with null volume of pores > 2 μm and a dominant pore size of 70 nm, which corresponded to an air-entry value of 4·1 MPa according to the Young–Laplace equation for capillary pressure (e.g. Bear, 2018). On unloading samples HM-1 and HM-2, an increase in the pore volume above 2 μm due to fissuring and some shifting of the lower dominant pore size mode (towards 100 nm) due to water absorption were observed compared to the intact material (Fig. 3(b)). On the contrary, the PSD of sample HM-3 in the same figure was remarkably similar to the PSD of the intact sample. Two important conclusions can be drawn from this last result. On the one hand, the drained loading path to 6 MPa – mainly developed in the pre-yield domain – did not induce a significant change in the shape of the PSD. However, the fast (undrained) unloading and the following freeze-drying process allowed the shape of the PSD to be kept at the maximum stress. This result is significant because the post-test techniques used to observe the microstructural changes after gas injection and without stress constraints will also be performed on rapidly unloaded samples (water undrained) using freeze-drying.

The same stress paths were followed on samples trimmed with bedding planes parallel to the axis of revolution. Fig. 4 compares the deformation response along different HM paths carried out at two sample orientations. Samples tested with bedding planes parallel to the axis displayed a higher stiffness during the first water undrained loading paths due to elastic anisotropy features (Fig. 4(a)). Fig. 4(b) presents the swelling behaviour of the samples during the flooding stage until they stabilise over time. Samples with bedding planes orthogonal to the axis of revolution displayed higher swelling strains, consistent with the higher compressibility on loading. As shown in Fig. 4(c), the effects of the inherent anisotropy were still observed on further drained loading in the pre-yield domain. This anisotropic behaviour is relevant since it influences the deformation response on gas injection and dissipation, as described in the following section.

Gas injection and dissipation tests. Permeability to gas

Water permeability under a controlled gradient was measured after the drained loading to $\sigma_v = 6{\cdot}0$ MPa and before the gas test (water pressures of 0·6 MPa at the bottom boundary, and 0·5 MPa at the top cap; point '2' in Fig. 2 on the right). Afterwards, the water pressure at the bottom boundary was decreased to 0·5 MPa until pore pressure equalisation.

After the withdrawal of water from the bottom cap, gas (air) was injected at this boundary at 0·5 MPa while keeping a constant $\sigma_v = 6{\cdot}0$ MPa large enough to avoid air passage between the sample and the oedometer ring. Preliminary tests were run to detect this passage of air through the sample–ring interface, in which a clear air pressure drop was detected once this interfacial pathway occurred when the air pressure exceeded the total radial stress (Gonzalez-Blanco, 2017). Liu *et al.* (2016a) indicated that gas migration through the interface only occurred when the gas pressure was more significant than the total radial stress. Therefore, to better understand this interface phenomenon, the coefficient of lateral earth pressure at rest K_0 on unloading was determined starting at OCR = 1. K_0 values increased with OCR, as shown in Fig. 5. K_0^{NC} results at OCR = 1 – reported in the figure – allowed estimation of the total horizontal stress before the air injection tests, with values of 5·2 MPa for bedding planes orthogonal to the flow and 4·5 MPa for flow

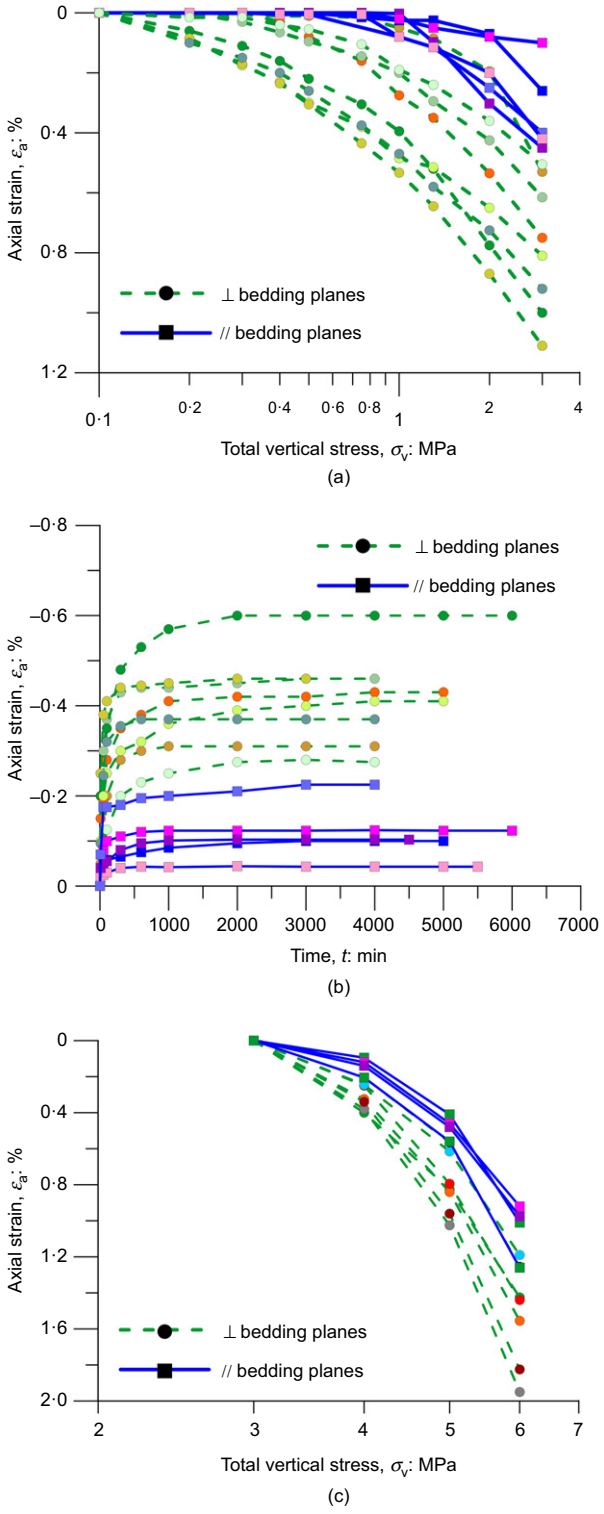

Fig. 4. Deformation response of samples with bedding planes orthogonal and parallel to the axis of revolution: (a) loading at constant water content ('AB' in Fig. 3(a)); (b) soaking at constant total vertical stress ('BC' in Fig. 3(a)); (c) drained loading ('CD' in Fig. 3(a))

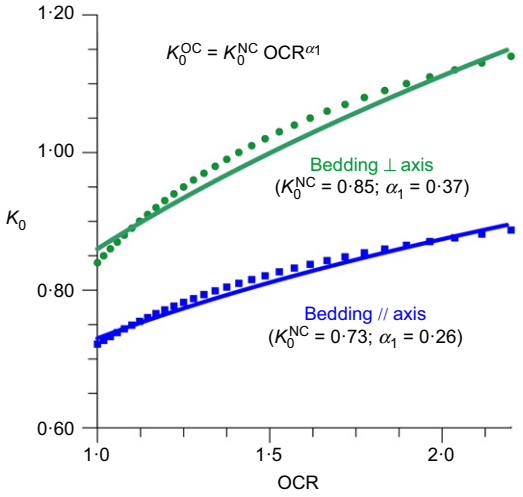

Fig. 5. Evolution of K_0 with overconsolidation ratio (OCR) at two different orientations: experimental data (symbols) and fitting (continuous line) using the equation and parameters shown in the figure

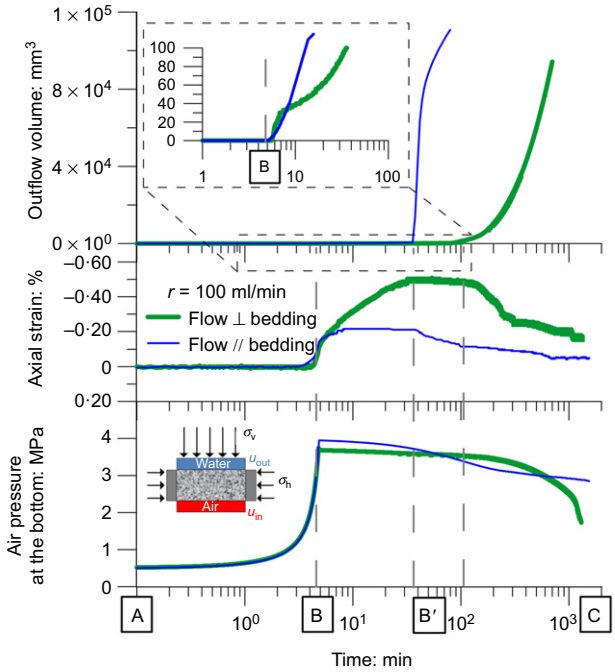

Fig. 6. Time evolutions of outflow volume, average axial strain and air pressure during the gas injection/dissipation tests at $r = 100$ ml/min. Samples with bedding planes parallel (thin lines) and orthogonal (thick lines) to gas flow. 'AB': air injection ramp; 'B': shut-off; 'BC': dissipation. Zoomed area in the upper graph from 1 to 100 min to better observe the initial outflow volume (mm^3)

parallel to bedding orientation. Therefore, air flow across the ring–sample interface was discarded because the maximum air pressure at the bottom boundary was limited to 4 MPa.

The air injection was applied at two different volume rates ($r = 100$ ml/min and 2 ml/min) while keeping a constant fluid pressure at the top boundary of 0·5 MPa. The selected rates were relatively fast to minimise diffusion of dissolved air through the saturated clayey matrix and to enhance two-phase flow mechanisms through pathways (effective diffusion coefficients of dissolved hydrogen in saturated BC are around 5×10^{-10} m^2/s (e.g. Jacops *et al.*, 2013, 2015)). These high gas injection rates (100 ml/min) were successfully used and interpreted in previous studies on low-permeability claystone formations reported by Romero *et al.* (2012), Senger *et al.* (2014, 2018) and Gonzalez-Blanco *et al.* (2022). Figs 6 and 7 present selected results for both orientations, and for $r = 100$ ml/min and $r = 2$ ml/min, respectively. These tests were chosen from a total of 12 injection tests performed at the same stress conditions and injection rates.

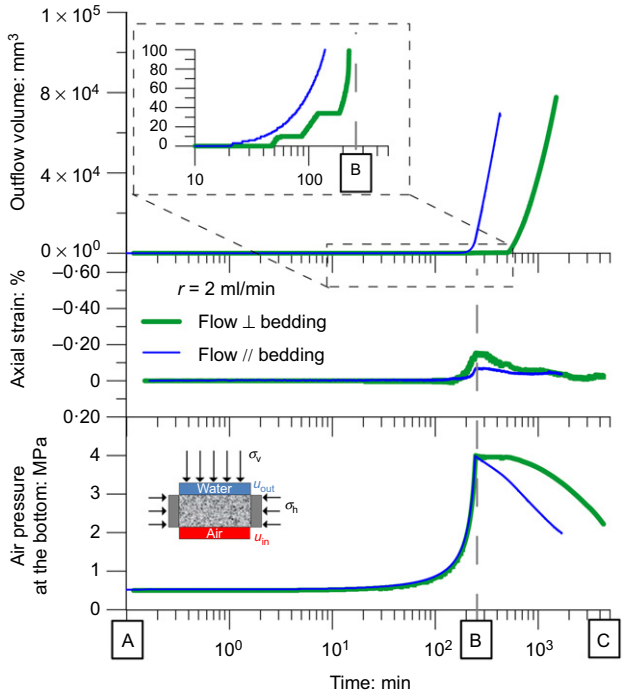

Fig. 7. Time evolutions of outflow volume, average axial strain and air pressure during the gas injection/dissipation tests at $r = 2$ ml/min. Samples with bedding planes parallel (thin lines) and orthogonal (thick lines) to gas flow. 'AB': air injection ramp; 'B': shut-off; 'BC': dissipation. Zoomed area in the upper graph from 10 to 500 min to better observe the initial outflow volume (mm^3)

When air pressure reached a maximum of 4 MPa (slightly below the initial air-entry value reported in Table 1) starting from the same initial air inlet volume and air pressure (air injection ramp 'AB' in Figs 6 and 7), the air injection piston was stopped (shut-off at 'B'), allowing pressure decay at a constant air volume of the inlet line (stage 'BC').

Samples at $\sigma_v = 6{\cdot}0$ MPa displayed some small expansion that induced degradation during the air injection ramp 'AB'. After shut-off, the deformational response differed depending on the air injection volume rates. At the faster rate ($r = 100$ ml/min) shown in Fig. 6, expansion/degradation continued at the shut-off stage as the air pressure front propagated into the sample ('BB′'), inducing the pore fluid pressure to increase at constant total vertical stress. After maximum expansion, the air injection pressure started to decline along the dissipation stage towards point 'C' with a sharp increase of the outflow volume through the top cap (upper plot in the figure). During the air dissipation stage, progressive compression of the material was recorded at constant total vertical stress and decreasing pore pressure.

At the slower injection rate shown in Fig. 7 ($r = 2$ ml/min), the sample underwent a slightly different evolution of deformation by displaying the entire expansion during the injection ramp and reaching the maximum swelling strain at the maximum air pressure 'B'. The slow injection rate allowed the equalisation of the pore pressure during air injection. The first outflow detection in the slow injection tests occurred during the injection stage (as indicated in the upper plot of the figure) when gas pathways reached the top of the sample.

The data also reflected the anisotropic deformation behaviour of BC depending on the bedding orientation. Samples with bedding planes orthogonal to flow systematically presented more expansion on air injection and larger compression on dissipation, consistent with the higher compressibility on soaking and loading detected in the previous HM paths.

Different procedures were followed to approximately discriminate the air and water volumetric proportions of the outflow volume: (*a*) determination of the final degrees of saturation after water undrained unloading; (*b*) indirect estimation of the volume of air by the perfect gas law in the closed outflow line; and (*c*) indirect determination of the volume of water by comparing their initial and final volumes in the outflow line. Procedures (*b*) and (*c*) were affected by the dead volumes of the outflow system. For example, after the dissipation test on the sample with the bedding planes parallel to the flow at 100 ml/min, the water displaced out of the sample was approximately 900 mm^3, while the total outflow volume accumulated in the PVC reached around $8{\cdot}3 \times 10^4$ mm^3 (i.e. approximately 1·1% corresponded to displaced water). Therefore, most of the outflow volume was associated with air.

Gas transport was expected to occur through localised pathways (Gonzalez-Blanco *et al.*, 2016) different to the connected pore network associated with water. A global air permeability k_a was determined under steady-state conditions during the dissipation stage using the generalised Darcy's law for compressible fluid and the entire sample area. The air pressure at the inlet changed from 4·0 MPa to around 1·5 MPa, during which pathway closure was expected, consistent with recorded compressive deformation. The low diffusion contribution of dissolved air through the saturated clayey matrix was neglected (around 3×10^{-8} (kg/s)/m^2 according to simulations reported by Gonzalez-Blanco *et al.* (2016)). The pressure decay method (e.g. Arnedo *et al.*, 2013; Pineda *et al.*, 2014) required the constant volume V of the upstream reservoir (dead and piston volumes) at varying absolute pressures $\bar{u}_a$, as well as the constant downstream pressure $\bar{u}_{at}$ at the top cap. The evolution of the absolute pressure decay $d\bar{u}_a/dt$ was recorded and used to estimate the mass of gas flowing through the sample assuming the perfect gas law.

$$k_a = \frac{k_i k_r \rho_a \boldsymbol{g}}{\mu_a} = -\frac{2L\,V \rho_a \boldsymbol{g}}{A\left(\bar{u}_a^2 - \bar{u}_{at}^2\right)} \frac{d\bar{u}_a}{dt} \tag{1}$$

$$k_i k_r = -\frac{2\mu_a L\,V}{A\left(\bar{u}_a^2 - \bar{u}_{at}^2\right)} \frac{d\bar{u}_a}{dt} \tag{2}$$

where k_i is the intrinsic permeability; k_r is the relative permeability to air ($k_i k_r$ represents the effective permeability to air, independent of fluid properties, as a measure of the ability of this phase to flow in the presence of water); A and L are the cross-sectional area and length of the sample; μ_a is the air dynamic viscosity at standard temperature and pressure; ρ_a is the air density at standard temperature and pressure; and $\boldsymbol{g}$ is the acceleration of gravity. $k_i k_r$ was used because the degree of saturation of the material was not precisely known during the steady-state dissipation stage.

Figure 8 summarises the effective permeabilities to air and water as a function of the average void ratios during the measurement. Effective permeability to water refers to fully saturated conditions (i.e. intrinsic permeability). Two orientations were considered (flow orthogonal and parallel to bedding). The effective permeability to air did not depend on the void ratio (at least within the small range of natural variability studied) and displayed slightly higher values than water (around a factor of 2·2 with flow parallel to bedding). The differences in air and water effective permeabilities were mainly associated with the new fissures generated on gas injection as described in the sections 'Results and interpretation of the microstructural analyses' and 'Interpretation of

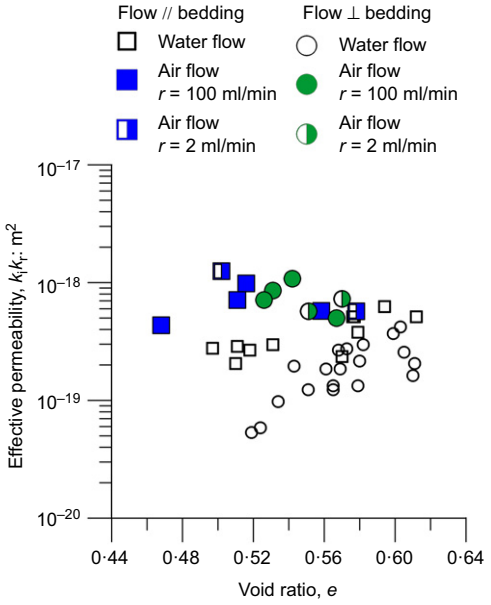

Fig. 8. Effective permeability to water and air against void ratio

the results within a multi-scale perspective'. Nevertheless, some differences could also be explained because of the pore pressure dependence on gas permeability of the Klinkenberg slippage effect (Klinkenberg, 1941), which is relevant when the intrinsic permeability is low ($< 10^{-18}$ m^2) or when the average pore pressure is low (e.g. Tanikawa & Shimamoto, 2006; Zimmerman, 2018). Furthermore, no anisotropic features were detected for effective permeabilities to air, which was not the case for water – higher intrinsic permeabilities were systematically observed when bedding planes were parallel to flow, consistent with previous results reported by Lima (2011).

Microstructural techniques after the gas injection tests

Three different techniques were used and interpreted to study the changes in the microstructure before and after the gas tests and to assess the creation of fissures during gas transport quantitatively; namely, the MIP as mentioned above, FESEM (e.g. Cotecchia *et al.*, 2016) and μCT (e.g. Andò *et al.*, 2012; Cnudde & Boone, 2013; Paul *et al.*, 2019). All these techniques were performed without stress constraints on fast unloaded samples (in the same way as in path 'DE' of test HM-3 in Fig. 3(a)) and with freeze-drying, which is required for MIP and FESEM. Although μCT did not require pre-treatment, the same freeze-drying process was applied to all samples to compare results. The preliminary HM-3 test (Fig. 3(b)) showed that the BC sample loaded to 6 MPa could preserve the PSD at this maximum stress and prevent fissure opening due to the high air-entry value of BC reported in Table 1. A significant decrease in this air-entry value and the impossibility of sustaining the high suction induced during water undrained stress relief would be expected if fissures/pathways were developed during gas injection. This low air-entry value scenario would allow better detection under unstressed conditions of the fissures/pathways formed.

Representative sub-samples for microstructural analyses were carefully trimmed from a core in an intact state and from seven oedometer degraded specimens after the gas injection tests. Two different shapes were considered: a cubical shape (for MIP and FESEM studies) and a cylindrical shape (for μCT tests to avoid corner artefacts),

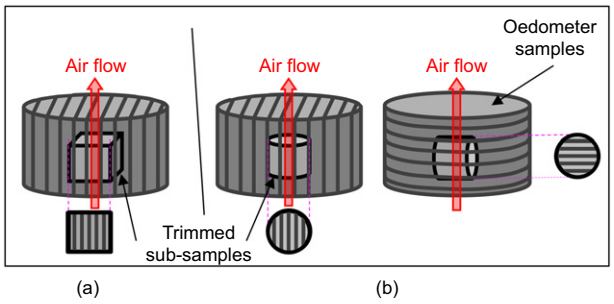

Fig. 9. Schematic diagrams illustrating trimming of sub-samples with different orientations for the microstructural studies

as shown in Fig. 9. Cubical samples of 1000 mm^3 were trimmed for performing the MIP tests, in which two different orientations were studied, namely, samples with gas flow orthogonal and parallel to bedding planes. Fig. 9(a) shows the specific case of a cubical sample retrieved from an oedometer specimen with gas flow parallel to the bedding planes. In the case of the FESEM, the cubical sample shown in Fig. 9(a) was trimmed with the peel-off surface scanned under the microscope at the top to better observe the bedding planes. Fig. 9(b) also presents the two orientations considered for μCT scanning when cutting the cylindrical samples after the gas tests with flow parallel and orthogonal to the bedding planes. The size of these cylindrical samples was limited to 15 mm dia. and 15 mm high to display an adequate μCT resolution (typically around 1/1000 of the object's cross-section diameter).

RESULTS AND INTERPRETATION OF THE MICROSTRUCTURAL ANALYSES

Figure 10 presents the PSDs (log–log plots) obtained with MIP for the intact material and after the gas injection tests. Most of the porosity was connected with cumulative intruded void ratios ranging from 0·43 and 0·59. A new family of large pores, which was not detected on intact samples, was consistently observed after the gas tests in both sample orientations. These new pore sizes larger than 2 μm were associated with the formation of gas pathways/fissures that increased the intrinsic permeability to gas (Gonzalez-Blanco *et al.*, 2016). These pore sizes were similar to those observed on drained unloading (tests HM-1 and HM-2 in Fig. 3(b)). As observed in Fig. 10, the volume of fissures (area under the PSD curves for $x > 2$ μm) did not significantly depend on gas flow direction. This evidence was consistent with the measured effective gas permeability that displayed an isotropic response.

Figure 11 shows FESEM micrographs of the intact sample and after the gas injection test at $r = 100$ ml/min with bedding planes normal to flow. The image of the scanned surface of the intact sample showed a relatively homogeneous material, and fissures were not observed at the selected magnification (Fig. 11(a)). However, several fissures could be distinguished in the micrograph of the sample after the gas injection at the same magnification (Fig. 11(b)). Most of them seemed to follow the predominant direction indicated in the figure (dashed white line), although some fissures were developing between the predominant ones (Fig. 11(c)). It was considered that gas flowed through these low-aperture discontinuities, connecting large-aperture fissures that follow the bedding planes (predominant direction). μCT results will be discussed later to support this observation. The separation of fissures in the predominant direction ranged between 150 nm and 270 nm. Higher magnifications at

different locations were also performed on the same sample after gas injection to measure the aperture of these fissures (Figs 11(c) and 11(d)), which ranged between 3 μm and 10 μm. These apertures were in the lower range of the new family of pore sizes detected by MIP (> 2 μm).

μCTs were performed on four cylindrical samples using 720 projections on 360° with a voxel size of 20 μm; namely, two samples at the intact state and two after the gas tests (r = 100 ml/min), and in both cases with bedding planes oriented orthogonal and parallel to the axis of revolution (Fig. 9(b)). Each set of cross-sections was analysed by identifying the main features and reconstructing the three-dimensional (3D) volume using the software ImageJ (Schneider *et al.*, 2012). Fig. 12 presents the volume reconstructions of the four samples, together with a vector

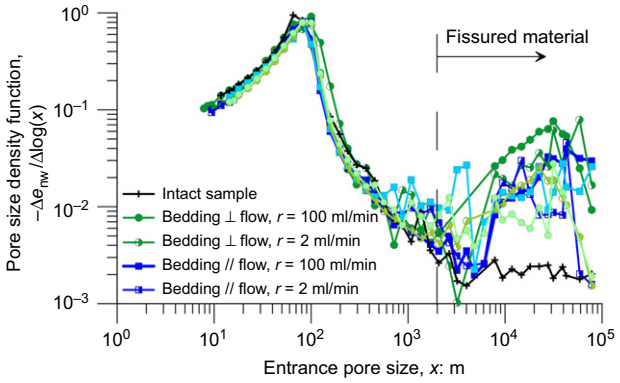

Fig. 10. Pore size density functions from MIP on the intact sample and after gas tests with bedding planes orthogonal to flow (circle symbols) and parallel to flow (square symbols)

indicating the gas flow direction and the orientation of the bedding planes (only for samples after the gas tests).

Figure 13 depicts three slices that correspond to the intact material and two samples after being tested at 100 ml/min with bedding planes parallel and orthogonal to flow. Since no noticeable differences were found between the two orientations of the intact samples, a single sample was finally selected to interpret the results (intact sample with bedding planes orthogonal to the sample axis, Fig. 13(a)). Calcium carbonate concretions or pyrite inclusions – in white due to their higher density – were detected in all the samples. Even though these natural discontinuities exist, the intact sample did not display any fissures or bedding planes (at least within the resolution adopted). On the contrary, some fissures were detected in the cross-sections after the gas injection tests. These fissures developed throughout the bedding planes and are encircled in the figure.

Samples after gas injection were analysed with the multi-scale Hessian fracture filtering (Voorn *et al.*, 2013) to isolate their fissure network, quantify their volumes better and assess their connectivity through a Matlab script. The different steps of the multi-scale Hessian fracture filtering – preparation, calibration and screening – were performed according to Voorn *et al.* (2013). Fig. 14 shows one slide of each sample before (input image) and after the filtering process, in which the fissure network, induced on gas injection, developed along nearly parallel traces coinciding with the bedding planes. Apertures smaller than the μCT resolution could not be observed, so FESEM (with better resolution) and μCT should be considered as complementary, covering different fissure sizes.

These large-aperture fissures throughout the sample were better visualised with 3D volume reconstructions. Fig. 15 shows the fissure pattern and the 3D volume of the original input stack of images for samples on both

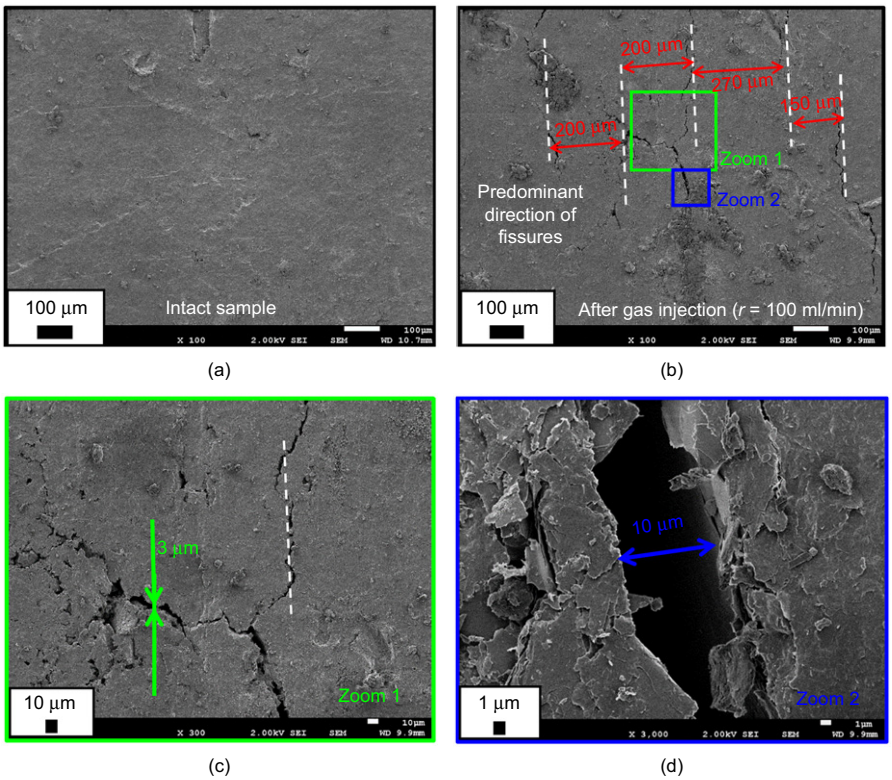

Fig. 11. Field-emission scanning electron microscopy (FESEM) micrographs: (a) intact sample; (b) sample after the gas test (r = 100 ml/min with bedding planes normal to flow) at the same magnification of (a); (c) and (d) zoomed areas 1 and 2, respectively, corresponding to two different locations on the sample after the gas test (b)

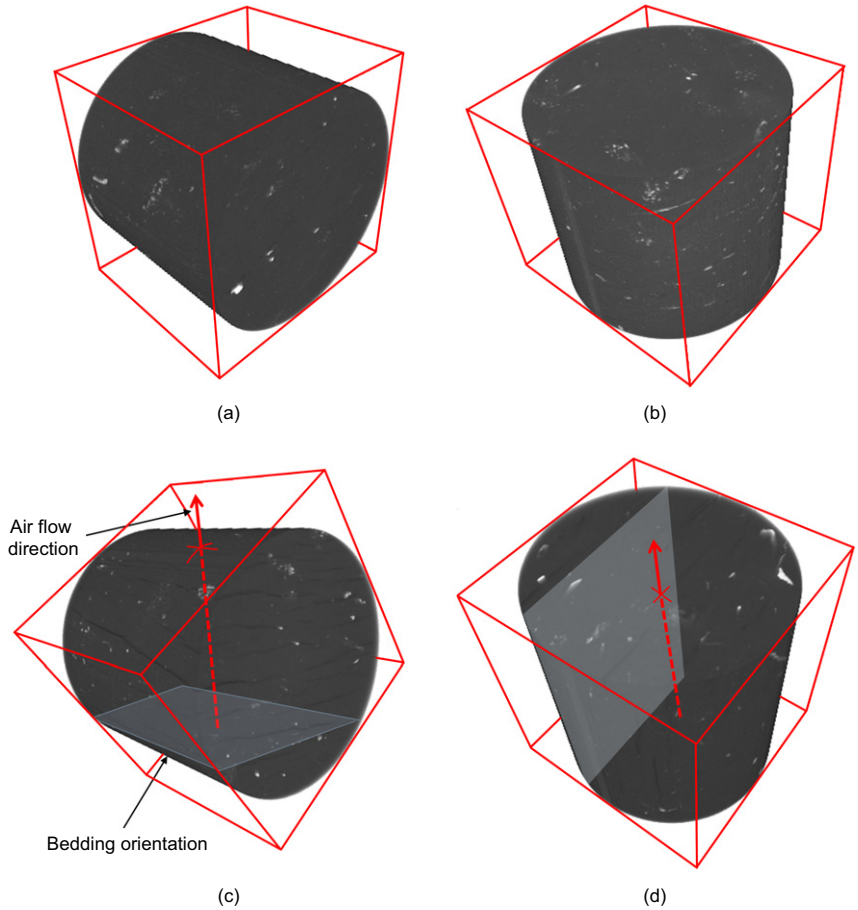

Fig. 12. Micro-focus X-ray computed tomography (μCT) volume reconstructions: (a) intact sample with bedding planes orthogonal to the sample axis; (b) intact sample with bedding planes parallel to the sample axis; (c) sample after the gas test with bedding planes orthogonal to flow; (d) sample after the gas test with bedding planes parallel to flow. $r = 100$ ml/min in both last cases

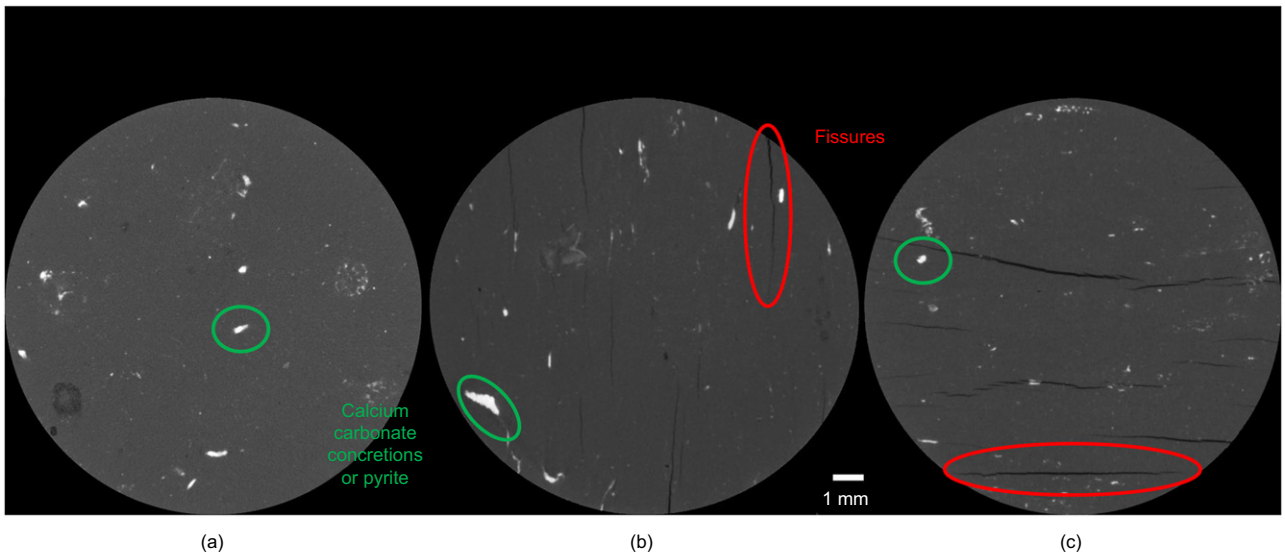

Fig. 13. Micro-focus X-ray computed tomography (μCT) images (a) of intact sample; (b) after the gas tests with bedding planes parallel to flow and (c) orthogonal to flow ($r = 100$ ml/min in both of the latter cases)

orientations. These volume reconstructions showed that gas flowed by way of the bedding planes. This fact is evident for bedding planes parallel to gas injection flow. However, the mechanism for gas transport with bedding planes orthogonal to flow appeared to be driven by low-aperture fissures (not resolved with μCT but observed in FESEM and MIP) that intersect no perfectly parallel bedding planes (resolved with μCT).

The Hessian fracture filtering also provided the capability of obtaining the connectivity of the large-aperture fissures (>40 μm; i.e. 2 voxels size) throughout the sample height in the direction orthogonal to the cross-sectional images

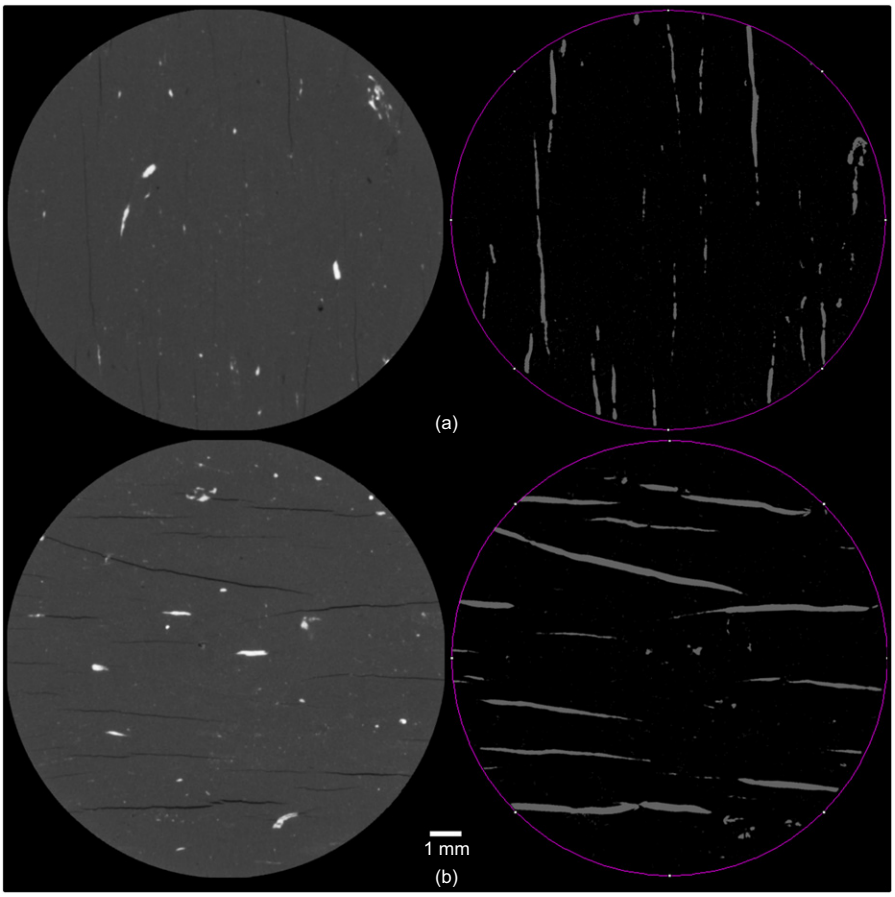

Fig. 14. Original input image (left) and after filtering process (right): (a) sample with bedding planes parallel to flow; (b) sample with bedding planes orthogonal to flow. $r = 100$ ml/min in both cases

(i.e. thought to be applied on a sample with gas flow parallel to bedding planes).

Figure 16 shows the 3D reconstruction of the connected fissures (on the left), the entire fissure volume (in the middle) and the overlapping with the whole volume of the sample (on the right). The reconstruction showed that only a small fraction of the volume of the large-aperture fissures was connected throughout the sample length. It was expected that, upon air injection, the pathways expanded and became connected, but during dissipation and sample compression, they closed again. Therefore, it was assumed that some volume of the connected porosity (within the μCT resolution) was not detected.

The 3D volume reconstruction also allowed the total and connected volumes of the network of the large-aperture fissures to be quantified using the 3D Object Counter plugin (Bolte & Cordelières, 2006). Table 2 summarises the total volume of the samples and the total and connected volumes of fissures for both orientations. The fissured volume resulted in 34·45 mm^3 for the sample with bedding planes parallel to flow, but only 25% of the fissures were connected throughout the sample length (Gonzalez-Blanco *et al.*, 2017). The fissured volume of the sample with bedding planes orthogonal to flow was lower, at 13·92 mm^3, and the connectivity of fissures in this orientation was not analysed since low-aperture fissures connecting bedding planes were not resolved with μCT.

The aperture, b, of large fissures and separation, a, detected with μCT were also assessed. The statistical analyses of the Fiji–ImageJ software allowed these values to be determined once the fissures with the 3D Objects Counter plugin were isolated. The aperture was determined as the double distance between the object's geometric centre to its surface. The separation was calculated as the minimum distance between two objects. Fig. 17 shows the histogram of fissure apertures and their mean values for samples with bedding planes parallel and orthogonal to flow. Fig. 18 displays the frequency distribution of fissure separations and their mean values for the two orientations. The results showed that fissures displayed a lower mean aperture but developed more closely together on the sample with bedding planes parallel to flow. The oedometer condition restricted the radial displacement of the sample and, therefore, the aperture b parallel to flow. A significant value to assess is the fissure density, a/b, which is the multiplicative inverse of the fissure volume per unit volume.

Experimental results of the current study on b, a and a/b are summarised in Table 3 for the different microstructural techniques. The large-aperture fissure results reported with μCT indicated larger mean separations than FESEM observations. These differences between techniques were associated with their resolution. As observed, a/b values reported with μCT were remarkably similar, which indicated no significant orientation effects in terms of fissure volume per unit volume of soil.

The μCT produced valuable information on the fissure network. However, to build a complete framework of understanding, MIP and FESEM data with better resolution should be considered to complement the information. For the sample with bedding planes parallel to flow, some volume of low-aperture fissures was not resolved by μCT. In the case of the sample with bedding planes orthogonal to flow, the mechanism for gas transport was not entirely captured by μCT since only large-aperture fissures in the bedding direction were detected. The schematic diagram in Fig. 19 for both sample orientations describes this interpretation. In

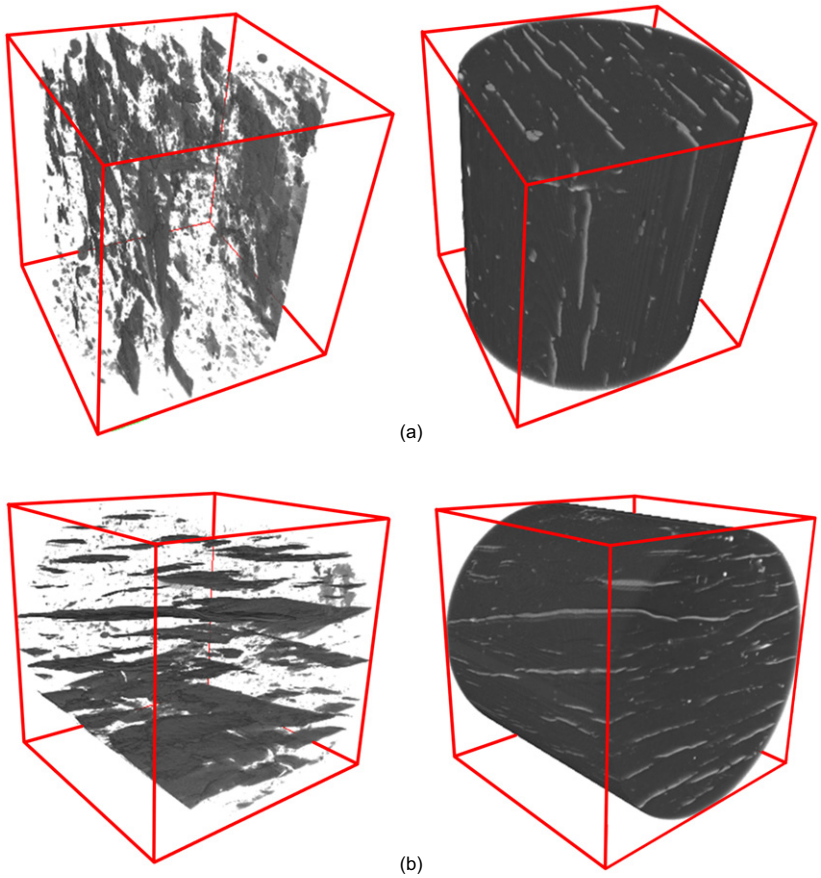

Fig. 15. Three-dimensional reconstruction of the fissure pattern: (a) sample with bedding planes parallel to flow after filtering process (left), and overlapped with the 3D volume of the input stack (right); (b) sample with bedding planes orthogonal to flow after filtering process (left) and overlapped with the 3D volume of the input stack (right). $r = 100$ ml/min in both cases

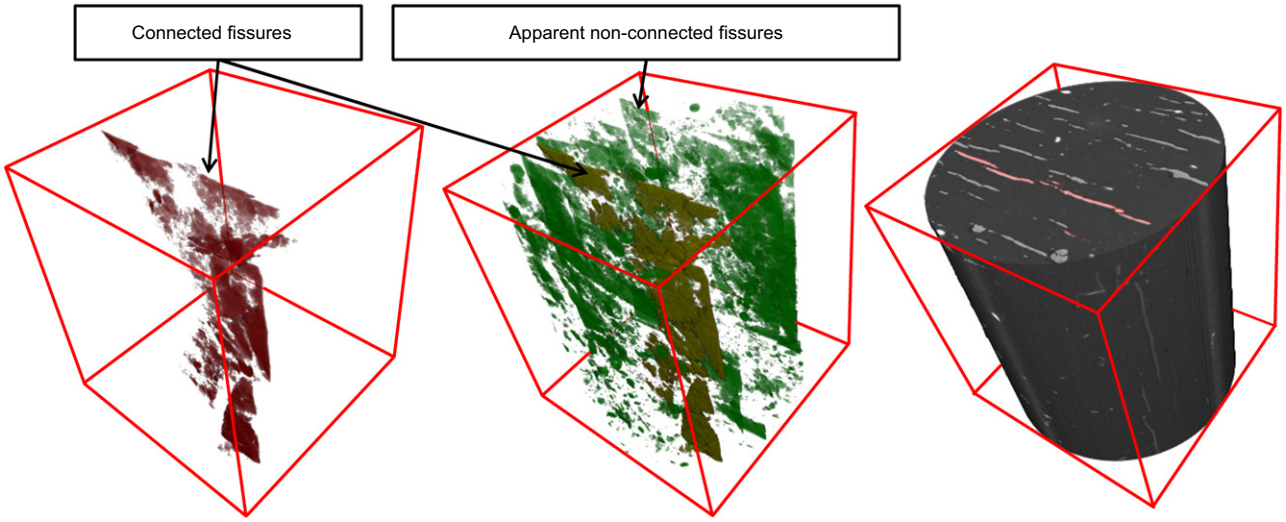

Fig. 16. Three-dimensional reconstruction of the connected fissure pattern after connectivity filtering (left); connected and non-connected fissure patterns (middle); and fissure pattern overlapped to the 3D volume of the input stack (right) for the sample with bedding planes parallel to flow at $r = 100$ ml/min

the case of flow orthogonal to bedding planes, low-aperture fissures connecting bedding planes were expected to be generated, as detected in FESEM images (Fig. 11(c)) and MIP. The volume of undetected fissures should be added to the bedding planes' volume resolved by μCT since, according to MIP, no differences in the fissured volume were detected at different orientations.

INTERPRETATION OF THE RESULTS WITHIN A MULTI-SCALE PERSPECTIVE

To assess the evolution of BC's intrinsic permeability and air-entry properties from the microstructural viewpoint, a more straightforward approach was followed based on the fissured volume that does not significantly depend on the orientation of the bedding planes. This volume is associated

Table 2. Total volume of the sample, total and connected volume of the large-aperture fissures $b > 40$ μm (μCT data)

Volumes	Sample with bedding // flow	Sample with bedding ⊥ flow
V_{total}: mm^3	1925	1596
$V_{fissures}$: mm^3	34·45	13·92
$V_{connected\ fissures}$: mm^3	8·59	*

*The orientation of the fissures precluded the application of the connectivity filter.

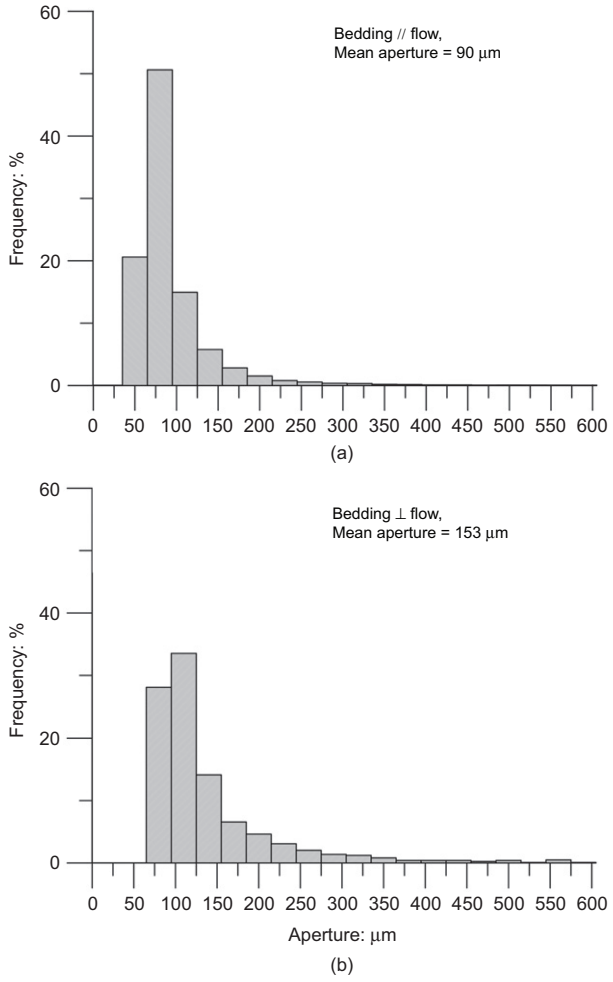

Fig. 17. Frequency of fissure apertures detected with μCT: (a) sample with bedding planes parallel to flow; (b) sample with bedding planes orthogonal to flow. $r = 100$ ml/min in both cases

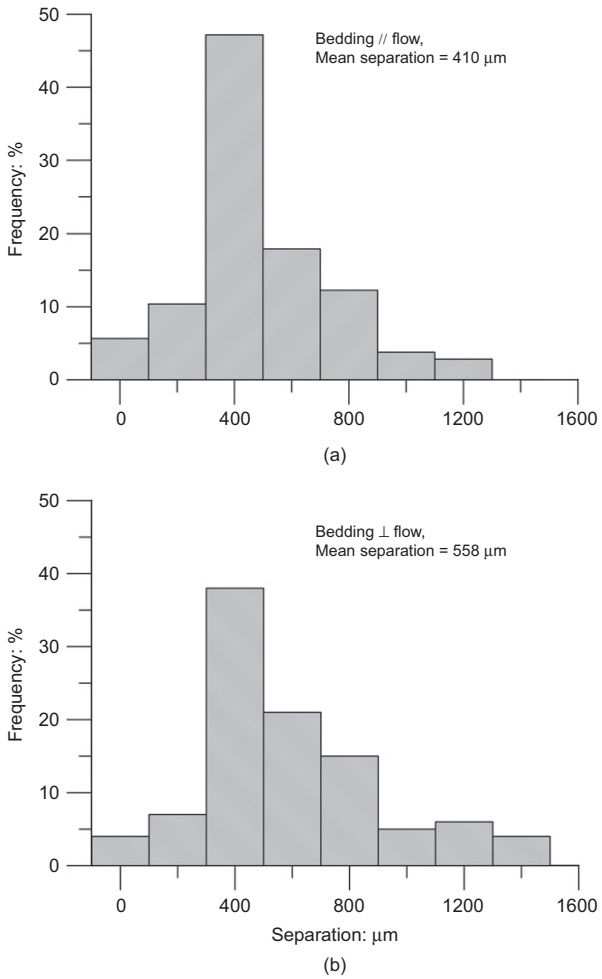

Fig. 18. Frequency of fissure separations detected with μCT: (a) sample with bedding planes parallel to flow; (b) sample with bedding planes orthogonal to flow. $r = 100$ ml/min in both cases

Table 3. Fissure apertures and separations using different microstructural techniques

Geometric properties	MIP	FESEM	μCT (large-aperture fissures)
Aperture, b: μm	>2	3–10	$90^{//}$–$153^{\perp}$
Separation, a: μm	—	150–270	$410^{//}$–$558^{\perp}$
Density of fissures, a/b	—	—	$4{\cdot}6^{//}$–$3{\cdot}6^{\perp}$

Note: $^{//}$ indicates mean values for the sample with bedding planes parallel to flow; $^{\perp}$ indicates mean values for the sample with bedding planes orthogonal to flow.

with the progressive degradation undergone by the material during air injection. Some modelling approaches use this mechanical degradation to capture the damage-induced increase in intrinsic permeability (e.g. Pereira & Arson, 2013; Fall *et al.*, 2014; Yang & Fall, 2021).

With this aim, a fissured void ratio $e_{fissured}$ – volume of fissures to volume of solids – was defined as the area in between the PSD curves obtained by MIP of the intact sample and after the gas tests for pore sizes $b > 2$ μm (Fig. 20). The volume of fissures ($b > 40$ μm) obtained after the filtering process of the μCT results was also computed and expressed in terms of $e_{fissured}$. The fissure volume per unit volume of soil, b/a, can be linked to the fissured void ratio through $e_{fissured} \propto b/a(1+e)$, where e is the void ratio that embraces fissures and pores. The volume of fissures to the volume of voids – fissured fraction $e_{fissured}/e$ – was also determined.

Table 4 shows the mean $e_{fissured}$ and $e_{fissured}/e$ values for $b > 2$ μm and $b > 40$ μm, as well as the results for 2 μm $< b \leq 40$ μm, obtained by MIP. Values for $b > 2$ μm did not display significant differences in either of the orientations. MIP and μCT results of $e_{fissured}$ with bedding planes parallel to flow were relatively consistent for $b > 40$ μm. However, μCT values were lower than MIP data ($b > 40$ μm) when the flow was orthogonal to the bedding planes. The $e_{fissured}$ detected by MIP and not resolved by μCT (2 μm $< b \leq 40$ μm) was higher when the flow was orthogonal to the bedding planes, which was in agreement with the undetected low-aperture fissures by μCT connecting the

bedding planes. The total $e_{fissured}$ by MIP ($2\ \mu m < b \leq 40\ \mu m$) and μCT ($b > 40\ \mu m$) was slightly larger with bedding planes parallel to flow. To make the calculations presented below straightforward, only MIP data for $b > 2\ \mu m$ were used to evaluate $e_{fissured}$ and $e_{fissured}/e$ values and relate them to the macroscopic gas transport properties. The fissured fraction was also helpful in providing information on the expected value of the final degree of saturation after the gas tests, $S_r = 1 - e_{fissured}/e$ reported in Table 4 when all fissures were desaturated.

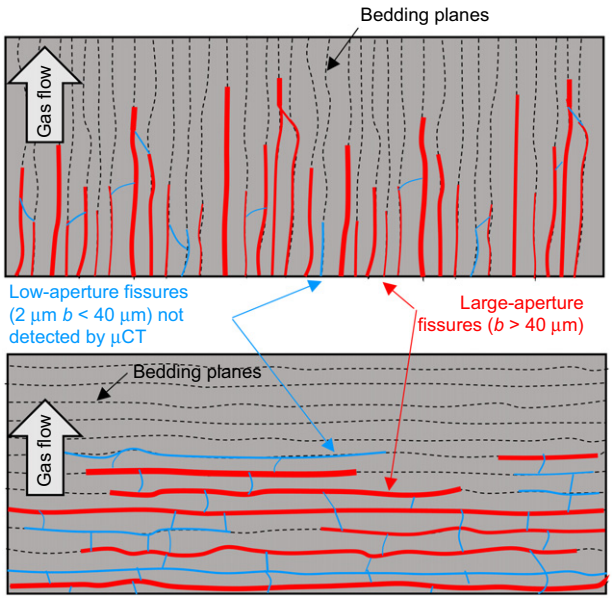

Fig. 19. Schematic representation of expected gas flow at different orientations of bedding planes: parallel to flow (top) and orthogonal to flow (bottom). Dashed thin lines represent bedding planes. Solid lines depict the volume occupied by gas: apertures larger than 40 μm and detected by μCT (thick lines); and apertures between 2 and 40 μm detected by MIP but not by μCT (thin lines)

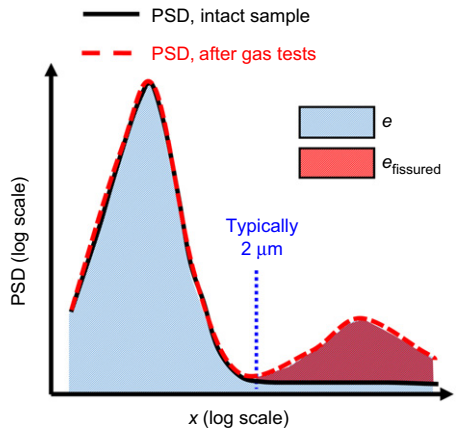

Fig. 20. Schematic representation of the fissured void ratio using PSD curves from MIP

The MIP data were processed according to the procedure explained in Romero *et al.* (1999) and Romero & Simms (2008) to obtain the water retention curves of intact samples and after the gas tests at high degrees of saturation. The results are plotted in Fig. 21 for matric suction (the figure includes experimental points obtained with the psychrometer and corrected with the osmotic component). After the gas injection tests, measurements of the degree of saturation of the clay (computed from the measured water contents and bulk densities) ranged between 0·89 and approximately 1, which are close to the values reported in Table 4 and confirmed the hypothesis of desaturated fissures. The air-entry values (matric suction) were estimated from the fitted water retention curves according to a unimodal van Genuchten-based model and corresponding to $S_r = 0{\cdot}95$. Fig. 22(a) presents data on the decrease of the air-entry value, and Fig. 22(b) the corresponding increase in intrinsic permeability, plotted against $e_{fissured}/e$ detected by MIP ($b > 2\ \mu m$). Intrinsic permeability was considered to represent the desaturated gas pathways (i.e. the relative permeability to gas was assumed to equal one). The intrinsic permeability of the undamaged (intact) material was based on water permeability results under full saturation reported in Fig. 8 (mean value of $2{\cdot}4 \times 10^{-19}$ m^2 for flow orthogonal to bedding and $4{\cdot}4 \times 10^{-19}$ m^2 for flow parallel to bedding without any correction for Klinkenberg effect).

A damage variable D can be introduced based on this fissured fraction (ratio of the fissured fraction to the maximum fissured fraction), which affects the macroscopic gas transport properties

$$D = \left(\frac{e_{fissured}}{e}\right) \Big/ \left(\frac{e_{fissured}}{e}\right)_{max} \tag{3}$$

with a maximum fissured fraction $(e_{fissured}/e)_{max} = 0{\cdot}101$ shown in Fig. 22.

The damage-induced change in intrinsic permeability k_i, plotted in Fig. 23(a), is determined as the sum of the intrinsic permeability of the undamaged BC k_{UD} (slightly dependent on void ratio within the studied range) and the isotropic damage enhanced permeability k_D (e.g. Fall *et al.*, 2014)

$$k_i = k_{UD} + k_D = k_{UD} + D(k_{max} - k_{UD}) \tag{4}$$

where $k_{max} = 1{\cdot}25 \times 10^{-18}$ m^2 is the maximum intrinsic permeability of the damaged BC (assuming complete

Table 4. Fissured void ratio, fissured ratio and degree of saturation using MIP (mean values from all tests) and μCT data for different aperture ranges

Sample	Technique	Aperture range	$e_{fissured}$	$e_{fissured}/e$	S_r
Bedding // flow ($e = 0{\cdot}560$)	MIP	$b > 2\ \mu m$	0·039	0·070	0·930
	MIP	$b > 40\ \mu m$	0·025	0·045	0·955
	MIP	$2\ \mu m < b \leq 40\ \mu m$	0·014	0·025	0·975
	μCT	$b > 40\ \mu m$	0·028	0·050	0·950
	MIP + μCT	$2\ \mu m < b \leq 40\ \mu m + b > 40\ \mu m$	0·042	0·075	0·925
Bedding ⊥ flow ($e = 0{\cdot}563$)	MIP	$b > 2\ \mu m$	0·041	0·073	0·927
	MIP	$b > 40\ \mu m$	0·020	0·036	0·964
	MIP	$2\ \mu m < b \leq 40\ \mu m$	0·021	0·037	0·963
	μCT	$b > 40\ \mu m$	0·014	0·025	0·975
	MIP + μCT	$2\ \mu m < b \leq 40\ \mu m + b > 40\ \mu m$	0·035	0·062	0·938

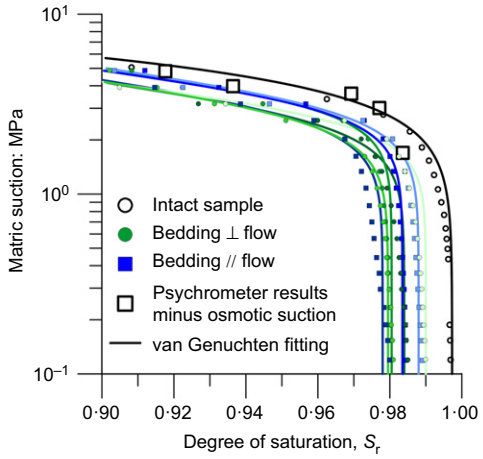

Fig. 21. Water retention curves in terms of matric suction of intact sample (using MIP and psychrometer results) and after the gas tests with different orientations using MIP data (isolated symbols) and fitting to unimodal van Genuchten's model (solid lines)

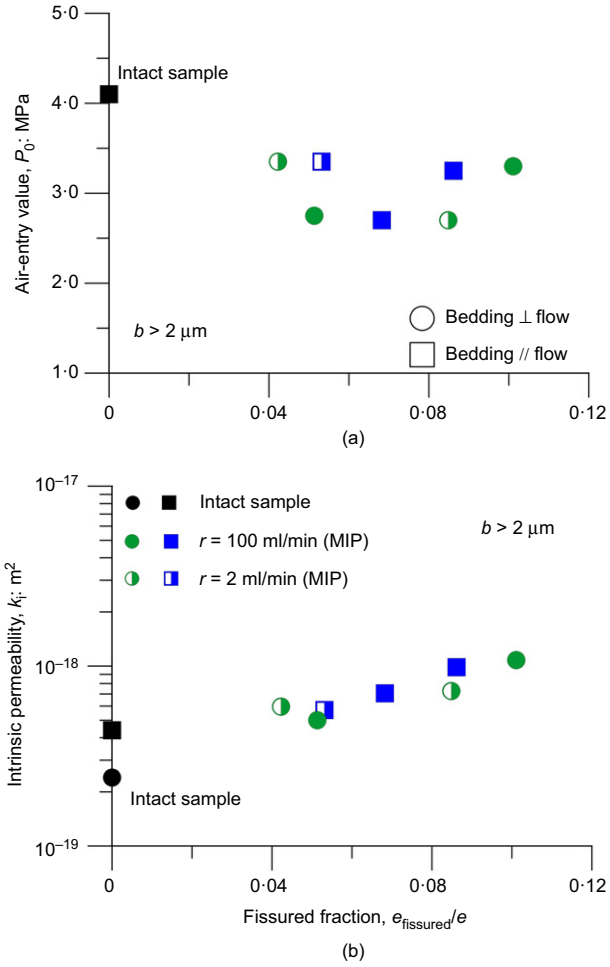

Fig. 22. Evolutions of (a) air-entry value and (b) intrinsic permeability with the fissured ratio

desaturation of the gas pathways in Fig. 8); and $k_{UD} = 3{\cdot}40 \times 10^{-19}$ m^2 represents the mean value of intrinsic permeability based on water permeability without any correction for the Klinkenberg effect. The k_{UD} was close to the reference value reported by Gonzalez-Blanco *et al.* (2016) of $4{\cdot}2 \times 10^{-19}$ m^2 at the reference in situ porosity and for an

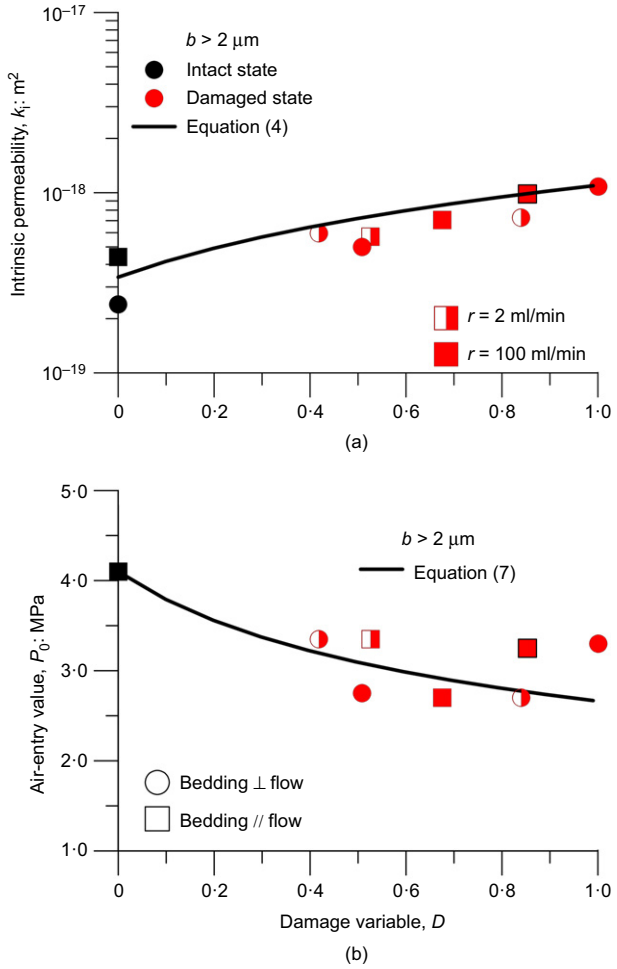

Fig. 23. Evolutions of (a) intrinsic permeability and (b) air-entry value with the damage variable. Fitted curves

initial aperture of fissures of 100 nm (equivalent to the dominant pore size of the intact material). This smooth increase in intrinsic permeability is associated with the fissure surface roughness and the tortuosity of the pathways.

The air-entry value P_0 (matric suction), plotted in Fig. 23(b), can be assessed by combining the Young–Laplace equation for parallel plates (e.g. Bear, 2018) and the cubic law of intrinsic permeability for smooth-walled parallel plates, which depend on the fissure aperture. The following expression for P_0 can be obtained with a parameter $\beta = 1/3$ (e.g. Olivella & Alonso, 2008) for a reference air-entry value $P_{0UD} = 4{\cdot}1$ MPa of the undamaged material (refer to Table 1)

$$P_0 = P_{0UD}\left[\frac{k_{UD}}{k_i}\right]^{\beta} \tag{5}$$

The air-entry pressure at the fissured state can be obtained combining equations (4) and (5)

$$\frac{k_i}{k_{UD}} = 1 + D\left(\frac{k_{max}}{k_{UD}} - 1\right) = 1 + \chi D \text{ with } \chi = 2{\cdot}7 \tag{6}$$

$$P_0 = P_{0UD}(1 + \chi D)^{-\beta} \tag{7}$$

Parameter $\beta = 0{\cdot}4$ (close to 1/3) was used to fit experimental results presented in Fig. 23(b).

Using the microstructural techniques described in the paper also enabled a wide range of pore sizes to be covered,

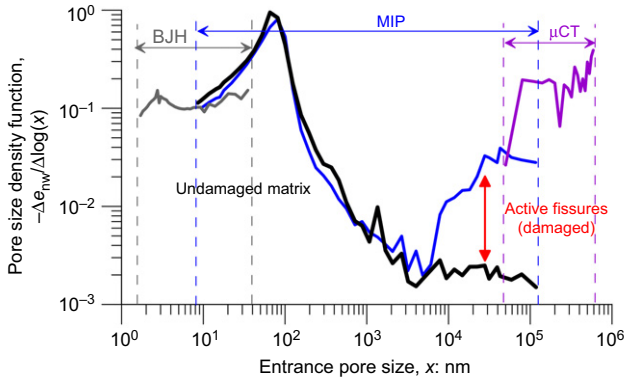

Fig. 24. Pore size density functions of the intact sample and after the gas tests combining three different techniques

from nanometre to millimetre scales. Although some authors have reported contradicting geometrical concepts in pore size analyses when using different techniques (e.g. Münch & Holzer, 2008), their combination better highlights the different features observed across scales. Fig. 24 shows this combination in terms of the PSD, in which different techniques (nitrogen-adsorption, MIP and μCT) have been plotted. The PSD allows the definition of a range of unaffected porosity (for pore sizes lower than 2 μm) that corresponds to the undamaged clay, in stark contrast to the development of fissures due to gas transport.

SUMMARY AND CONCLUDING REMARKS

This paper has presented experimental results using a multi-scale and HM coupled methodology related to gas transport in saturated deep BC. Gas injection and dissipation tests under oedometer conditions and constant total vertical stress (close to in situ effective vertical stress) were performed at different air volume injection rates and on samples with oriented bedding planes – parallel and orthogonal to axial flow.

The sharp increase in the gas outflow volume at the maximum expansion during air pressurisation and the higher effective permeability to air during the gas dissipation stage (compared to water permeability results before the air tests) indicated the development of preferential pathways (fissures) across the specimen. Moreover, the effective air permeability did not significantly depend on the orientation of the sample.

The microstructural study after air tests was performed with complementary techniques, which confirmed the opening of fissures with different apertures and separations. In addition, MIP results allowed a new family of fissures >2 μm to be identified that did not depend on the orientation and were consistent with the measured isotropic response of the effective gas permeability. Image processing using μCT confirmed the opening of fissures with large apertures (>40 μm) mainly developing along the weaker bedding planes. This technique detected lower mean apertures and closer mean separations with bedding planes parallel to axial flow. However, the density of fissures was similar in both orientations, which coincided with the observations of MIP results.

The mechanism for gas transport with bedding planes orthogonal to flow appeared to be driven by low-aperture fissures (detected by MIP and FESEM but not with μCT) with narrower separations connecting no perfectly parallel bedding planes. Therefore, it was considered that these inter-bedding and low-aperture pathways were also very efficient in terms of gas transport since the effective permeability to air indicated no clear anisotropic features. Furthermore, data from the different techniques were consistent despite their different resolutions, since MIP and μCT analyses resulted in similar fissured void ratios for sizes >40 μm for bedding planes parallel to axial flow.

At the end of the paper, an effort was made to combine MIP data (fissured void ratio) and the phenomenological results after the gas tests (air-entry value and intrinsic permeability of the fissured medium). Experimental data showed decreased air-entry value and increased intrinsic permeability with rising fissured ratios. Therefore, expressions using a damage variable derived in terms of the fissured fraction and the undamaged properties were proposed to assess these degradation-induced changes affecting gas transport properties. However, further experimental research is needed to validate this damage law at different stresses and maximum gas pressures since modifying these variables will induce different mechanical degradations that affect the macroscopic gas transport properties.

ACKNOWLEDGEMENTS

The authors are grateful to ONDRAF/NIRAS (Belgian National Agency for Radioactive Waste and Enriched Fissile Material) for funding this research programme under contract no. XSI/AV/2012-1952 (2012–2016) and no. CCHO 2018-0089/00/00 (2018–2020). This project has received funding from the European Union's Horizon 2020 research and innovation programme 'European Joint Programme on Radioactive Waste Management' EURAD (2019-2024) WP-Gas 'Mechanistic understanding of gas transport in clay materials' under the grant agreement No. 847593. The Spanish 'Severo Ochoa Programme for Centres of Excellence in R&D' (CEX2018-000797-S) is also acknowledged.

NOTATION

A	area of the sample
a	fissure separation
a/b	density of fissures
B	isotropic pore pressure parameter for incompressible solid
b	fissure aperture
D	damage variable
D_s	fractal dimension
e	void ratio
$e_{fissured}$	fissured void ratio – volume of fissures to the volume of solids
$e_{fissured}/e$	fissured fraction – volume of fissures to the volume of voids
e_{nw}	non-wetting void ratio (mercury intrusion porosimetry (MIP))
$e_{nw\,max}$	maximum connected void ratio
$\boldsymbol{g}$	acceleration of gravity
K_0	coefficient of lateral earth pressure at rest
K_0^{NC}	coefficient of lateral earth pressure at rest at normally consolidated conditions
k_a	air permeability
k_D	damage enhanced intrinsic permeability
k_i	intrinsic permeability
$k_i k_r$	effective permeability
k_{max}	maximum intrinsic permeability of the damaged state
k_r	relative permeability
k_{UD}	undamaged intrinsic permeability
L	length of the sample
n	porosity
P_0	air-entry value (matric suction)
P_{0UD}	air-entry value of the undamaged state (matric suction)
r	volumetric air injection rate
S_r	degree of saturation

s total suction
t time
$\bar{u}_a$ absolute air pressure of the upstream reservoir
$\bar{u}_{at}$ absolute air pressure of the downstream reservoir
u_{in} fluid pressure at the inlet
u_{out} fluid pressure at the outlet
u_w pore water pressure
V volume of the upstream reservoir
$V_{connected\ fissures}$ volume of connected fissures
$V_{fissures}$ volume of fissures
V_{total} volume of the sample
w water content
w_L liquid limit
w_P plastic limit
x entrance pore size
α parameter of van Genuchten's equation
α_1 parameter that controls the evolution of K_0 with overconsolidation ratio
β parameter combining Young–Laplace equation and the intrinsic permeability
ε_a axial strain
λ parameter of van Genuchten's equation
μ_a air dynamic viscosity at standard pressure and temperature
π osmotic suction
ρ soil bulk density
ρ_a air density at standard pressure and temperature
ρ_d soil dry density
ρ_s density of solids
σ_h total horizontal stress
σ_v total vertical stress
χ parameter controlling the rate of decrease of P_0 with damage in equation (6)

REFERENCES

Andò, E., Bésuelle, P., Hall, S. A., Viggiani, G. & Desrues, J. (2012). Experimental micromechanics: grain-scale observation of sand deformation. *Géotech. Lett.* **2**, No. 3, 107–112, https://doi.org/10.1680/geolett.12.00027.

Arnedo, D., Alonso, E. E. & Olivella, S. (2013). Gas flow in anisotropic claystone: modelling triaxial experiments. *Int. J. Numer. Analyt. Met.* **37**, No. 14, 2239–2256, https://doi.org/10.1002/nag.2132.

Bear, J. (2018). *Modeling phenomena of flow and transport in porous media*, Springer Series on Theory and Applications of Transport in Porous Media, vol. 31. Cham, Switzerland: Springer.

Bernier, F., Bastiaens, W. & Li, X. L. (2007). Twenty-five years' geotechnical observation and testing in the Tertiary Boom Clay formation. *Géotechnique* **57**, No. 2, 229–237, https://doi.org/10.1680/geot.2007.57.2.229.

Bésuelle, P., Viggiani, G., Desrues, J., Coll, C. & Charrier, P. (2014). A laboratory experimental study of the hydromechanical behavior of Boom Clay. *Rock Mech. Rock Engng* **47**, No. 1, 143–155, https://doi.org/10.1007/s00603-013-0421-8.

Bolte, S. & Cordelières, F. P. (2006). A guided tour into subcellular colocalisation analysis in light microscopy. *J. Microsc.* **224**, No. 3, 213–232, https://doi.org/10.1111/j.1365-2818.2006.01706.x.

Brosse, A. M., Jardine, R. J. & Nishimura, S. (2017). The undrained shear strength anisotropy of four Jurassic to Eocene stiff clays. *Géotechnique* **67**, No. 8, 653–671, https://doi.org/10.1680/jgeot.15.P.227.

Cevatoglu, M., Bull, J. M., Vardy, M. E., Gernon, T. M., Wright, I. C. & Long, D. (2015). Gas migration pathways, controlling mechanisms and changes in sediment acoustic properties observed in a controlled sub-seabed CO_2 release experiment. *Int. J. Greenh. Gas Control* **38**, 26–43, https://doi.org/10.1016/j.ijggc.2015.03.005.

Cnudde, V. & Boone, M. N. (2013). High-resolution X-ray computed tomography in geosciences: a review of the current technology and applications. *Earth-Sci. Rev.* **123**, 1–17, https://doi.org/10.1016/j.earscirev.2013.04.003.

Cotecchia, F., Cafaro, F. & Guglielmi, S. (2016). Microstructural changes in clays generated by compression explored by means of SEM and image processing. *Procedia Engng* **158**, 57–62, https://doi.org/10.1016/j.proeng.2016.08.405.

Cui, L. Y., Ye, W. M., Wang, Q., Chen, Y. G., Chen, B. & Cui, Y. J. (2020). Insights into determination of gas breakthrough in saturated compacted Gaomiaozi bentonite. *J. Mater. Civ. Engng* **32**, No. 7, 04020190, https://doi.org/10.1061/(ASCE)MT.1943-5533.0003206.

Cuss, R., Harrington, J., Giot, R. & Auvray, C. (2014). Experimental observations of mechanical dilation at the onset of gas flow in Callovo-Oxfordian claystone. *Geol. Soc. Spec. Publ.* **400**, No. 1, 507–519, https://doi.org/10.1144/SP400.2.

Damians, I. P., Olivella, S. & Gens, A. (2019). Modelling a gas flow experiment in Mx80 bentonite. In *Proceedings of the XVII European conference on soil mechanics and geotechnical engineering (ECSMGE 2019): geotechnical engineering, foundation of the future* (eds H. Sigursteinsson, S. Erlingsson, B. Bessason), pp. 629–699, https://doi.org/10.32075/17ECSMGE-2019-0692. Reykjavik, Iceland: Icelandic Geotechnical Society.

Dao, L. Q. (2015). *Etude du comportement anisotrope de l'argile de Boom*. PhD thesis, Universite Paris-Est, Paris, France (in French).

Delage, P., Audiguier, M., Cui, Y. J. & Howat, M. D. (1996). Microstructure of a compacted silt. *Can. Geotech. J.* **33**, No. 1, 150–158, https://doi.org/10.1139/t96-030.

Delage, P., Le, T. T., Tang, A. M., Cui, Y. J. & Li, X. L. (2007). Suction effects in deep Boom Clay block samples, *Géotechnique* **57**, No. 1, 293–244, https://doi.org/10.1680/geot.2007.57.2.239.

Delahaye, C. H. & Alonso, E. E. (2002). Soil heterogeneity and preferential paths for gas migration. *Engng Geol.* **64**, No. 2–3, 251–271, https://doi.org/10.1016/S0013-7952(01)00104-1.

EURAD (European Joint Programme on Radioactive Waste Management) (2019). *Mechanistic modelling of gas transport in clay materials*. Chatenay-Malabry, France: EURAD, Agence Nationale pour la gestion des Déchets Radioactifs (Andra). See https://www.ejp-eurad.eu/implementation/mechanistic-understanding-gas-transport-clay-materials-gas (accessed 08/08/2022).

Fall, M., Nasir, O. & Nguyen, T. S. (2014). A coupled hydro-mechanical model for simulation of gas migration in host sedimentary rocks for nuclear waste repositories. *Engng Geol.* **176**, 24–44, https://doi.org/10.1016/j.enggeo.2014.04.003.

Gerard, P., Harrington, J., Charlier, R. & Collin, F. (2014). Modelling of localised gas preferential pathways in claystone. *Int. J. Rock Mech. Min.* **67**, 104–114, https://doi.org/10.1016/j.ijrmms.2014.01.009.

Giger, S. B., Marschall, P., Lanyon, G. W. & Martin, C. D. (2015). Transferring the geomechanical behaviour of Opalinus Clay observed in lab tests and Mont Terri URL to assess engineering feasibility at potential repository sites. *Proceedings of the 49th U.S. rock mechanics/geomechanics symposium*, San Francisco, CA, USA, paper ARMA-2015-057.

Giraud, A. & Rousset, G. (1996). Time-dependent behaviour of deep clays. *Engng Geol.* **41**, No. 1–4, 187–195, https://doi.org/10.1016/0013-7952(95)00000-3.

Gonzalez-Blanco, L. (2017). *Gas migration in deep argillaceous formations: Boom Clay and indurated clays*. PhD thesis, Universitat Politècnica de Catalunya, Barcelona, Spain.

Gonzalez-Blanco, L., Romero, E., Jommi, C., Li, X. & Sillen, X. (2016). Gas migration in a Cenozoic clay: experimental results and numerical modelling. *Geomech. Energy Environ.* **6**, 81–100, https://doi.org/10.1016/j.gete.2016.04.002.

Gonzalez-Blanco, L., Romero, E., Jommi, C., Sillen, X. & Li, X. (2017). Exploring fissure opening and their connectivity in a Cenozoic clay during gas injection. In *Advances in laboratory testing and modelling of soils and shales (ATMSS)* (eds A. Ferrari and L. Laloui), pp. 288–295, https://doi.org/10.1007/978-3-319-52773-4_33. Cham, Switzerland: Springer.

Gonzalez-Blanco, L., Romero, E., Marschall, P. & Levasseur, S. (2022). Hydro-mechanical response to gas transfer of deep argillaceous host rocks for radioactive waste disposal. *Rock Mech. Rock Engng* **55**, 1159–1177, https://doi.org/10.1007/s00603-021-02717-3.

Gutiérrez-Rodrigo, V., Villar, M. V., Martín, P. L., Romero, F. J. & Barcala, J. M. (2015). Gas-breakthrough pressure of FEBEX bentonite. In *Gas generation and migration in deep geological radioactive waste repositories* (ed. R. P. Shaw), Geological

Society Special Publication no. 415, pp. 47–57, https://doi.org/10.1144/SP415.4. London, UK: The Geological Society.

Harrington, J. F. & Horseman, S. T. (1999). Gas transport properties of clays and mudrocks. *Geol. Soc. Spec. Publ.* **158**, No. 1, 107–124, https://doi.org/10.1144/GSL.SP.1999.158.01.09.

Harrington, J. F., Milodowski, A. E., Graham, C. C., Rushton, J. C. & Cuss, R. J. (2012). Evidence for gas-induced pathways in clay using a nanoparticle injection technique. *Mineral. Mag.* **76**, No. 8, 3327–3336, https://doi.org/10.1180/minmag.2012.076.8.45.

Harrington, J. F., Cuss, R. J. & Talandier, J. (2017). Gas transport properties through intact and fractured Callovo-Oxfordian mudstones. In *Geomechanical and petrophysical properties of mudrocks* (eds E. H. Rutter, J. Mecklenburgh and K. G. Taylor), Geological Society Special Publication no. 454, pp. 131–154, https://doi.org/10.1144/SP454.7. London, UK: The Geological Society.

Harrington, J. F., Graham, C. C., Cuss, R. J. & Norris, S. (2019). Gas network development in compact bentonite: key controls on the stability of flow pathways. *Geofluids* **2019**, article ID 3815095, https://doi.org/10.1155/2019/3815095.

Hildenbrand, A., Schlömer, S., Krooss, B. M. & Littke, R. (2004). Gas breakthrough experiments on pelitic rocks: comparative study with N_2, CO_2 and CH_4. *Geofluids* **4**, No. 1, 61–80, https://doi.org/10.1111/j.1468-8123.2004.00073.x.

Jacops, E., Volckaert, G., Maes, N., Weetjens, E. & Govaerts, J. (2013). Determination of gas diffusion coefficients in saturated porous media: He and CH_4 diffusion in Boom Clay. *Appl. Clay Sci.* **83–84**, 217–223, https://doi.org/10.1016/j.clay.2013.08.047.

Jacops, E., Wouters, K., Volckaert, G., Moors, H., Maes, N., Bruggeman, C., Swennen, R. & Littke, R. (2015). Measuring the effective diffusion coefficient of dissolved hydrogen in saturated Boom Clay. *J. Appl. Geochem.* **61**, 175–184, https://doi.org/10.1016/j.apgeochem.2015.05.022.

Jockwer, N. & Wieczorek, K. (2008). *Gas migration in the Opalinus Clay as a function of the gas injection pressure*, HG-C Project, Final Report GRS-249. Braunschweig, Germany: Gesellschaft für Anlagenund Reaktorsicherheit (GRS) mbH.

Keller, L. M., Holzer, L., Schuetz, P. & Gasser, P. (2013). Pore space relevant for gas permeability in Opalinus clay: statistical analysis of homogeneity, percolation, and representative volume element. *J. Geophys. Res. Solid Earth* **118**, No. 6, 2799–2812, https://doi.org/10.1002/jgrb.50228.

Klinkenberg, L. J. (1941). The permeability of porous media to liquids and gases. In *Drilling and production practices*, API-41-200, pp. 200–213. Washington, DC, USA: American Petroleum Institute.

Lima, A. (2011). *Thermo-hydro-mechanical behaviour of two deep Belgian clay formations: Boom and Ypresian clays*. PhD thesis, Universitat Politècnica de Catalunya, Barcelona, Spain.

Liu, J. F., Song, Y., Skoczylas, F. & Liu, J. (2016a). Gas migration through water-saturated bentonite–sand mixtures, COx argillite, and their interfaces. *Can. Geotech. J.* **53**, No. 1, 60–71, https://doi.org/10.1139/cgj-2014-0412

Liu, Z. B., Shao, J. F., Liu, T. G., Xie, S. Y. & Conil, N. (2016b). Gas permeability evolution mechanism during creep of a low permeable claystone. *Appl. Clay Sci.* **129**, 47–53, https://doi.org/10.1016/j.clay.2016.04.021.

Matthews, G. P., Levy, C. L., Laudone, G. M., Jones, K. L., Ridgway, C. J., Hallin, I. L., Gazze, S. A., Francis, L., Whalley, W. R., Schoelkopf, J. & Gane, P. A. C. (2018). Improved interpretation of mercury intrusion and soil water retention percolation characteristics by inverse modelling and void cluster analysis. *Transp. Porous Med.* **124**, No. 2, 631–653, https://doi.org/10.1007/s11242-018-1087-1.

Münch, B. & Holzer, L. (2008). Contradicting geometrical concepts in pore size analysis attained with electron microscopy and mercury intrusion. *J. Am. Ceram. Soc.* **91**, No. 12, 4059–4067, https://doi.org/10.1111/j.1551-2916.2008.02736.x.

Nguyen, V., Pineda, J. A., Romero, E. & Sheng, D. (2021). Influence of soil microstructure on air permeability in compacted clay. *Géotechnique* **71**, No. 5, 373–391, https://doi.org/10.1680/jgeot.18.P.186.

Olivella, S. & Alonso, E. E. (2008). Gas flow through clay barriers. *Géotechnique* **58**, No. 3, 157–176, https://doi.org/10.1680/geot.2008.58.3.157.

Paul, S., Roy, S., Ghosh, P., Zarandi, M. A., Cender, T. & Pillai, K. M. (2019). A novel method for permeability estimation from micro-tomographic images. *Transp. Porous Med.* **127**, No. 1, 171–190, https://doi.org/10.1007/s11242-018-1186-z.

Pereira, J. M. & Arson, C. (2013). Retention and permeability properties of damaged porous rocks. *Comput. Geotech.* **48**, 272–282, https://doi.org/10.1016/j.compgeo.2012.08.003.

Pineda, J. A., Romero, E., Alonso, E. E. & Pérez, T. (2014). A new high-pressure triaxial apparatus for inducing and tracking hydro-mechanical degradation of clayey rocks. *Geotech. Test. J.* **37**, No. 6, 933–947, https://doi.org/10.1520/GTJ20130163.

Romero, E. & Gonzalez-Blanco, L. (2015). *Complementary water and air permeability tests on core samples from Schlattingen SLA-1 borehole*, NAGRA Technical Report NAB 15-06. Wettingen, Switzerland: NAGRA.

Romero, E. & Simms, P. H. (2008). Microstructure investigation in unsaturated soils: a review with special attention to contribution of mercury intrusion porosimetry and environmental scanning electron microscopy. *Geotech. Geol. Engng* **26**, No. 6, 705–727, https://doi.org/10.1007/s10706-008-9204-5.

Romero, E., Gens, A. & Lloret, A. (1999). Water permeability, water retention and microstructure of unsaturated compacted Boom Clay. *Engng Geol.* **54**, No. 1–2, 117–127, https://doi.org/10.1016/S0013-7952(99)00067-8.

Romero, E., Senger, R., Marschall, P. & Gómez, R. (2012). Air tests on low-permeability claystone formations. Experimental results and simulations. In *Multiphysical testing of soils and shales* (eds L. Laloui and A. Ferrari), pp. 69–83, https://doi.org/10.1007/978-3-642-32492-5_6. Berlin/Heidelberg, Germany: Springer.

Salehnia, F., Collin, F., Li, X. L., Dizier, A., Sillen, X. & Charlier, R. (2015). Coupled modeling of excavation damaged zone in Boom Clay: strain localisation in rock and distribution of contact pressure on the gallery's lining. *Comput. Geotech.* **69**, 396–410, https://doi.org/10.1016/j.compgeo.2015.06.003.

Schneider, C. A., Rasband, W. S. & Eliceiri, K. W. (2012). NIH Image to ImageJ: 25 years of image analysis. *Nat. Methods* **9**, No. 7, 671–675, https://doi.org/10.1038/nmeth.2089.

Senger, R., Lanyon, B., Marschall, P., Vomvoris, S. & Fujiwara, A. (2008). Numerical modeling of the gas migration test at the Grimsel test site (Switzerland). *Nucl. Technol.* **164**, No. 2, 155–168, https://doi.org/10.13182/NT08-A4016.

Senger, R., Romero, E., Ferrari, A. & Marschall, P. (2014). Characterization of gas flow through low-permeability claystone: laboratory and two-phase flow analyses. In *Clays in natural and engineered barriers for radioactive waste confinement* (eds S. Norris, J. Bruno, M. Cathelineau, P. Delage, C. Fairhurst, E. C. Gaucher, E. H. Höhn, A. Kalinichev, P. Lalieux and P. Sellin), Geological Society Special Publication no. 400, pp. 531–543, https://doi.org/10.1144/SP400.15. London, UK: The Geological Society.

Senger, R., Romero, E. & Marschall, P. (2018). Modeling of gas migration through low-permeability clay rock using information on pressure and deformation from fast air injection tests. *Transp. Porous Med.* **123**, No. 3, 563–579, https://doi.org/10.1007/s11242-017-0962-5.

Sultan, N., Cui, Y. J. & Delage, P. (2010). Yielding and plastic behaviour of Boom Clay. *Géotechnique* **60**, No. 9, 657–666, https://doi.org/10.1680/geot.7.00142.

Tanikawa, W. & Shimamoto, T. (2006). Klinkenberg effect for gas permeability and its comparison to water permeability for porous sedimentary rocks. *Hydrol. Earth Syst. Sci. Discuss.* **3**, 1315–1338, https://doi.org/10.5194/hessd-3-1315-2006.

van Genuchten, M. (1980). A closed-form equation for predicting the hydraulic conductivity of unsaturated soils. *Soil Sci. Soc. Am. J.* **44**, No. 5, 892–898, https://doi.org/10.2136/sssaj1980.03615995004400050002x.

Villar, M. V., Romero, F. J., Martín, P. L., Gutiérrez-Rodrigo, V. & Barcala, J. M. (2019). Experimental investigation of gas transport in the shaly facies of Opalinus Clay. In *Energy geotechnics, SEG 2018* (eds A. Ferrari and L. Laloui), pp. 434–441, https://doi.org/10.1007/978-3-319-99670-7. Cham, Switzerland: Springer.

Volckaert, G., Mallants, D., Bush, R. A. & Lambers, L. (1998). Long-term environmental impact of underground disposal of

P&T waste. In *Proceedings of the fifth information exchange meeting on actinide and fission product partitioning and transmutation*, pp. 463–472. Mol, Belgium: SKC-CEN.

Voorn, M., Exner, U. & Rath, A. (2013). Multiscale Hessian fracture filtering for the enhancement and segmentation of narrow fractures in 3D image data. *Comput. Geosci.* **57**, 44–53, https://doi.org/10.1016/j.cageo.2013.03.006.

Webb, P. A. & Orr, C. (1997). *Analytical methods in fine particle technology*, vol. 301. Norcross, GA, USA: Micromeritics Instrument Corp.

Wiseall, A. C., Cuss, R. J., Graham, C. C. & Harrington, J. F. (2015). The visualisation of flow paths in experimental studies of clay-rich materials. *Mineral. Mag.* **79**, No. 6, 1335–1342, https://doi.org/10.1180/minmag.2015.079.06.09.

Yang, J. & Fall, M. (2021). Coupled hydro-mechanical modelling of dilatancy controlled gas flow and gas induced fracturing in saturated claystone. *Int. J. Rock Mech. Min. Sci.* **138**, 104584, https://doi.org/10.1016/j.ijrmms.2020.104584.

Zimmerman, R. W. (2018). *Fluid flow in porous media*, The Imperial College Lectures in Petroleum Engineering, vol. 5. London, UK: World Scientific Publishing Europe Ltd.